

IDENTIKIT 1: A MODELING TOOL FOR INTERACTING DISK GALAXIES

JOSHUA E. BARNES¹ AND JOHN E. HIBBARD²

¹ Institute of Astronomy, University of Hawaii, 2680 Woodlawn Drive, Honolulu, HI 96822, USA; barnes@ifa.hawaii.edu

² National Radio Astronomy Observatory, 520 Edgemont Road, Charlottesville, VA 22903, USA; jhibbard@nrao.edu

Received 2008 May 13; accepted 2008 November 8; published 2009 January 13

ABSTRACT

By combining test-particle and self-consistent techniques, we have developed a method to rapidly explore the parameter space of galactic encounters. Our method, implemented in an interactive graphics program³, can be used to find the parameters required to reproduce the observed morphology and kinematics of interacting disk galaxies. We test this system on an artificial data set of 36 equal-mass merging encounters, and show that it is usually possible to reproduce the morphology and kinematics of these encounters and that a good match strongly constrains the encounter parameters.

Key words: galaxies: interactions – galaxies: kinematics and dynamics – methods: *N*-body simulations

Online-only material: color figures

1. INTRODUCTION

The diverse morphological and kinematic features of interacting disk galaxies have a simple dynamical explanation: galactic bridges and tails (Toomre & Toomre 1972), rings (Lynds & Toomre 1976; Theys & Spiegel 1977), and related structures result when ordinary galactic disks experience strong tides in close encounters. Tides also cause interacting galaxies to merge by inexorably transferring energy and momentum from relative motion to internal degrees of freedom (Toomre 1977; White 1978; Barnes 1988). With such a straightforward physical basis, one might expect that dynamical modeling of interacting galaxies would be relatively easy. However, it is very time consuming to explore the large parameter space required to describe a galaxy collision and find a good match to the kinematics and morphology of a specific system. In addition, it has never been entirely clear that a good match yields a unique or physically meaningful model.

In this paper, we develop and test an efficient methodology to model the observable morphology and kinematics of pairs of interacting disk galaxies. Empirical tests show that the resulting models can be used to make strong inferences about the systems they match. While we do not consider minor mergers and interactions in this paper, our methodology can easily be extended to treat such encounters.

At first glance, it seems all too easy to model interacting galaxies—and impossible to do so with any degree of confidence. The dynamical state of a galactic collision is described by a phase-space distribution function, $f(\mathbf{r}, \mathbf{v})$, which gives the mass density at position \mathbf{r} and velocity \mathbf{v} . In contrast, observations of a specific component c (e.g., neutral hydrogen) yield a data cube $F_c(X, Y, V)$, which represents the distribution of that component at each point (X, Y) on the plane of the sky as a function of line-of-sight velocity V . Since $f(\mathbf{r}, \mathbf{v})$ depends on six variables, while $F_c(X, Y, V)$ depends on only three, it appears that observations do not provide enough information. Put simply, there are an infinite number of different six-dimensional distribution functions consistent with any given three-dimensional data cube.

On further reflection, the problem is not quite as hopeless as it appears. This is because a typical galaxy merger begins with a tidal encounter between two normal, fairly symmetric spirals. Galaxies are scrambled as they merge, but the stars and dark matter which constitute most of their mass evolve collisionlessly. The fundamental dynamical equation,

$$\frac{\partial f}{\partial t} + \mathbf{v} \cdot \frac{\partial f}{\partial \mathbf{r}} - \frac{\partial \Phi}{\partial \mathbf{r}} \cdot \frac{\partial f}{\partial \mathbf{v}} = 0, \quad (1)$$

where Φ is the gravitational potential, is fully reversible (e.g., van Albada & van Gorkom 1977); thus in some sense the original galaxies are still there, imposing a hidden symmetry on the dynamical state of a merging system. So we need not consider all possible distribution functions consistent with a given data cube; only a very small subset of these functions can possibly result from an encounter between two normal disk galaxies.

In practice, mergers are modeled by guessing initial conditions, numerically simulating the ensuing collision, and comparing the result with the morphology and kinematics of the system one wants to model. If the model fails to match the observations, one must go back and guess again until the results are satisfactory. Most of the guess work focuses on selecting the disk orientations, typically specified by angles (i_1, ω_1) and (i_2, ω_2) for disks 1 and 2 (Toomre & Toomre 1972); also needed are the eccentricity e and pericentric separation p of the initial orbit, as well as the galactic mass ratio μ . So seven parameters are needed to specify the initial conditions for an encounter of two axisymmetric disk galaxies—not counting the parameters used to specify their internal structures.⁴

Once a simulation has been run, one must select another nine parameters when comparing the results to observational data: a time t since pericenter, a viewing direction given, for example, by angles $(\theta_X, \theta_Y, \theta_Z)$, scale factors \mathcal{L} and \mathcal{V} for

⁴ Selecting the correct internal structures is a separate problem, and one largely beyond the scope of this paper. Under some fairly general assumptions, the internal structure of an axisymmetric galaxy may be described by a distribution function $f = f(E, J_z, I_3)$ depending on the energy E , angular momentum about the symmetry axis J_z , and a third integral of motion I_3 . Formally speaking, an infinite number of parameters are needed to specify such a function.

³ This software is available at <http://www.ifa.hawaii.edu/faculty/barnes/research/identikit/>.

length and velocity,⁵ a center-of-mass position on the plane of the sky ($X_{\text{cm}}, Y_{\text{cm}}$), and center-of-mass velocity V_{cm} . All told, a minimum of 16 parameters are needed to completely specify the initial conditions, time, point of view, and scale of a merger model. This plethora of parameters has long posed a challenge for systematic surveys of galactic collisions (Toomre & Toomre 1972; Farouki & Shapiro 1982; Wallin & Stuart 1992; Howard et al. 1993; Barnes 1998; Naab & Burkert 2003). The problem we address here is slightly different—instead of trying to survey the entire parameter space, we want to navigate toward a solution matching the morphology and kinematics of a given interacting system. Intuition and prior experience can guide this process by narrowing the range of parameter space explored. Nonetheless, given the size and complexity of this parameter space, it is not surprising that many simulations must be run to attempt a match, or that detailed models of galactic collisions are not easy to produce.

2. “IDENTIKIT” METHODOLOGY

While self-consistent simulations are useful to finalize dynamical models of tidally interacting galaxies, here we simulate galactic disks with test particles. Test particles have a long history (Pfleiderer & Seidentopf 1961; Toomre & Toomre 1972; Combes et al. 1980; Hernquist & Quinn 1987; Wallin & Stuart 1992) and nicely reproduce features such as bridges, tails, and shells which develop with little direct influence from self-gravity. To include orbital decay, which is crucial in modeling the more advanced stages of galaxy encounters and mergers, the test particles may be used to estimate the drag on the central masses (e.g., Toomre & Toomre 1972; Borne 1984; Quinn & Goodman 1986). However, orbit decay is largely driven by tidal interactions of galaxy *halos* (e.g., Toomre 1977; White 1978; Barnes 1988), and it is relatively easy to compute the self-consistent interaction of two halos using N -body simulations. Our initial approach was therefore to represent the mass of each galaxy with a spherical distribution of massive particles; in each of these spheres, we embedded *multiple* disks of test particles, and decided which disk was to be displayed *after* running the simulations.⁶

Building on this idea, and taking advantage of the faster processors now available, we have replaced these discrete collections of disks with spherical swarms of test particles moving on circular orbits—in effect, populating each galaxy model with *all* possible disks.

The modeling procedure begins by selecting mass models for the two galaxies, thereby fixing the mass ratio μ . Our models include a bulge, a disk, and a halo; these components have cumulative mass profiles $m_b(r)$, $m_d(r)$, and $m_h(r)$, respectively, where $m_c(r)$ is the total mass in component c within radius r . For each galaxy, we compute the total mass profile

$$m(r) = m_b(r) + m_d(r) + m_h(r), \quad (2)$$

calculate the corresponding isotropic distribution function using Eddington’s (1916) formula (e.g., Binney & Tremaine 1987, p. 236), and construct a spherical N -body realization of this

profile using N_{sphr} equal-mass particles. Details of this procedure are given in Appendix A.

Each of these spherical N -body realizations is then loaded with N_{test} test particles moving on circular orbits. We pick the orientation of the orbit of test particle i by randomly drawing its normalized angular momentum \hat{s}_i from a uniform distribution on the unit sphere \mathbf{S}^2 . The radial distribution of the test particles may be chosen at will. The simplest choice is to use a radial distribution following the cumulative profile of the disk, $m_d(r)$; with this approach, the test particles representing a disk with a normalized spin vector \hat{s}_d are those with

$$1 - \hat{s}_d \cdot \hat{s}_i \leq \sigma, \quad (3)$$

where $\sigma \ll 1$ is a tolerance parameter proportional to the number of particles selected. In practice, however, this places many disk particles at small radii where they are largely immune to tides. The sampling at large radii can be improved by radially biasing the test-particle distribution. We do this by multiplying the local disk particle density, $\rho_d(r) = (4\pi r^2)^{-1} dm_d/dr$, by a factor of r^2 , and replacing Equation (3) with

$$1 - \hat{s}_d \cdot \hat{s}_i \leq \sigma / \max(q_i, r_{\min})^2. \quad (4)$$

Here q_i is the *initial* orbital radius of particle i , and r_{\min} is a parameter which keeps Equation (4) from diverging for small q_i . Particles selected using Equation (4) follow the original disk distribution down to radius r_{\min} ; at smaller radii the disk is undersampled, but this has little effect if r_{\min} is small.

Finally, two such configurations are placed on a relative orbit with a given pericentric separation p and eccentricity e and followed until they merge; we save particle positions and velocities every few time steps, creating a database of several hundred frames tracing the system’s history from start to finish. These data can then be used to approximate *any* encounter with the chosen μ , p , and e .

Identikit software includes interactive routines allowing the user to select the disk orientations, viewing direction, scale factors, and centroid positions; the resulting test-particle coordinates are instantly projected on the (X, Y) , (X, V) , (V, Y) , and (X, Z) planes. The user can also step forward or backward in time, switch between databases created using different values for p , μ , or e , and vary the tolerance parameter σ . In addition, an observational data cube $F(X, Y, V)$ for a specific system, in order to be matched, may be projected onto the (X, Y) , (X, V) , and (V, Y) planes, typically using gray-scale or contour images. A laptop computer can easily store the necessary data and supply the modest processing power required when searching for a match. Figure 1 presents an example; the encounter and viewing parameters have been adjusted so the test particles (points) closely match the data cube (grayscale).

3. EXPERIMENTAL VALIDATION

The Identikit system is designed with the primary goal of analyzing observations. However, it is not straightforward to perform empirical tests using observational data. For one thing, much of the available data are rather heterogeneous; data sets with uniformly high resolution and signal-to-noise ratio are not easy to obtain. For another, we do not know the true initial conditions and viewing parameters for more than a handful of the mergers that have been observed, so we do not have any simple way to validate the results of our modeling. To determine if Identikit can actually reconstruct galactic encounters from the

⁵ If the simulation is conducted in physical units then these parameters are not necessary—but additional parameters are required to describe the initial conditions, so the total parameter count is unchanged.

⁶ In forensic investigations, “Identikit” is one of the several systems used to construct portraits by selecting from a menu of facial features. Our approach is analogous.

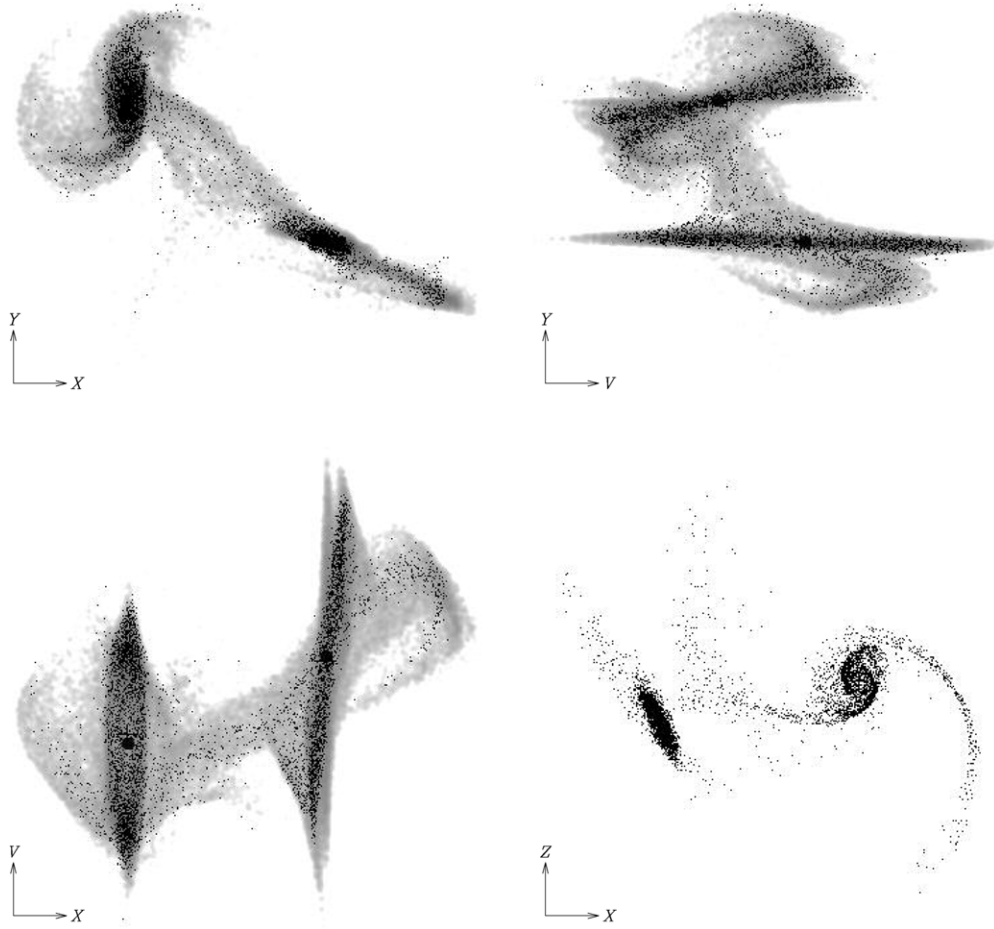


Figure 1. Identikit match to a pair of merging galaxies. Gray-scale images represent the data cube $F(X, Y, V)$ of the system, while points represent the Identikit model. Top-left, top-right, and bottom-left quadrants show the data cube and the model projected on the (X, Y) , (V, Y) , and (X, V) planes, respectively; the bottom-right quadrant shows the model projected on the (X, Z) plane.

information contained in data cubes, we tested it on an artificial data set of 36 self-consistent disk galaxy merger simulations with random orientations, times since first passage, viewing directions, and scale factors.

3.1. Artificial Merger Data

Our disk galaxy model has a spherical bulge (Hernquist 1990a) containing 5% of the mass, an exponential/isothermal disk (de Vaucouleurs 1959a, 1959b; Freeman 1970; van der Kruit & Searle 1981) containing another 15%, and a spherical dark halo (Navarro et al. 1996) containing the remaining 80%. The density profiles for these components are

$$\begin{aligned} \rho_b(r) &\propto r^{-1}(r + a_b)^{-3}, \\ \rho_d(q, z) &\propto e^{-q/a_d} \operatorname{sech}^2(z/z_d), \\ \rho_h(r) &\propto r^{-1}(r + a_h)^{-2}, \end{aligned} \quad (5)$$

where a_b is the scale length of the bulge, $q = \sqrt{x^2 + y^2}$ is the cylindrical radius, a_d is the scale length of the disk, z_d is the scale height of the disk, and a_h is the scale length of the halo. Each galaxy was realized using a total of $N = 131,072$ particles. The simulations used natural units with Newton's constant $G = 1$. In these units, the galaxy model has total mass $m = 1.25$ and half-mass radius $r_{\text{med}} \simeq 0.532$. The disk's scale length $a_d = 1/12$, and the median circular velocity of the disk material is $v_{\text{med}} \simeq 1.23$; at a radius of $3a_d$ the orbital period is $t_{\text{orb}} \simeq 1.23$.

We restricted our artificial data set to equal-mass ($\mu = 1$) encounters with parabolic initial orbits ($e = 1$); for each orbit, the pericentric separation p was drawn from a uniform distribution in the range $[0.05, 0.5] = [0.6, 6]a_d$. The instant when this idealized two-body orbit reaches the pericenter defines $t = 0$; times $t < 0$ are before pericenter, while times $t > 0$ are after pericenter. We adopt a coordinate system in which the orbital angular momentum vector is parallel to the \hat{z} axis. The normalized spin vector \hat{s} of each disk was chosen from a uniform distribution on the unit sphere S^2 ; in practice, the inclination i was chosen by drawing $\cos(i) = \hat{s} \cdot \hat{z}$ from a uniform distribution in the range $[-1, 1]$, and the argument ω was chosen from a uniform distribution in the range $[0^\circ, 360^\circ]$. Further details on the galaxy models and the merger simulations are given in [Appendix B](#).

For each of the 36 merger simulations we chose a random time between first and second pericenters, rescaled the system by random factors in length and velocity, and “observed” it from a random direction. We first determined the relative orbit of each pair of galaxies, using the most tightly bound 2048 particles in each bulge to measure galactic positions. Let $t_1 \simeq 0$ and t_2 be the times of first and second pericenters, respectively; the random time t was drawn from a uniform distribution in the range $[t_1, t_2]$ and rounded down to the nearest available output time.

Next, we selected scale factors \mathcal{L} and \mathcal{V} for length and velocity, respectively. These were chosen so that the galaxy models obey a mass–radius–velocity relation of the form $M \propto$

$R^2 \propto V^4$ with a small amount of scatter (see Tully & Fisher 1977). Let ξ be drawn from a uniform distribution in the range $[-0.5, 0.5]$, and g_1 and g_2 be drawn from a Gaussian distribution with zero mean and unit dispersion; then

$$\mathcal{L} = 10^{\xi/2} 10^{0.05g_1}, \quad \mathcal{V} = 10^{\xi/4} 10^{0.05g_2}. \quad (6)$$

Finally, we chose a random viewing direction $\hat{\mathbf{Z}}$ from a uniform distribution on the unit sphere \mathbf{S}^2 . We drew a second vector $\hat{\mathbf{X}}_0$ from the same distribution, and set $\hat{\mathbf{X}} = \hat{\mathbf{X}}_0 - \hat{\mathbf{Z}}(\hat{\mathbf{X}}_0 \cdot \hat{\mathbf{Z}})$ and $\hat{\mathbf{Y}} = \hat{\mathbf{Z}} \times \hat{\mathbf{X}}$. These vectors and scale factors were used to map the position \mathbf{r}_i and velocity \mathbf{v}_i of each particle i to data-cube coordinates:

$$X_i = \mathcal{L} \hat{\mathbf{X}} \cdot \mathbf{r}_i, \quad Y_i = \mathcal{L} \hat{\mathbf{Y}} \cdot \mathbf{r}_i, \quad V_i = \mathcal{V} \hat{\mathbf{Z}} \cdot \mathbf{v}_i. \quad (7)$$

Particles from the disks of the two galaxies, transformed to (X_i, Y_i, V_i) coordinates, provide an N -body representation of a data cube $F_d(X, Y, V)$ for the disk material. Such data are roughly comparable to the neutral hydrogen data cubes $F_{\text{HI}}(\alpha, \delta, V_{\text{los}})$ available for many interacting galaxies (e.g., Hibbard et al. 2001). The simulated data have better resolution than most observational data sets and are free of noise and interferometric artifacts; moreover, our simulations used collisionless particles instead of neutral gas. We could have run random mergers with gas to improve the correspondence between the simulations and real observational data, but the computing time required for a large suite of simulations with gas is non-trivial. Fortunately, collisionless simulations do a good job of reproducing the tidal features commonly detected in H I since the latter usually evolve ballistically once tidally extracted from their parent galaxies.

To present the simulated data in the form required for Identikit matching, we projected the disk particles for each of our 36 mergers on the (X, Y) , (X, V) , and (V, Y) planes; gridded particle distributions were lightly smoothed to produce gray-scale images. We also used tightly bound particles from the bulge of each galaxy to determine its position and line-of-sight velocity; the results were plotted on top of the gray-scale images. Our images are thus analogous to H I maps supplemented with accurate nuclear coordinates and velocities.

The entire procedure outlined above, including both the generation of the simulations and the selection of viewing parameters, was performed by automated scripts without human intervention; we did not know the actual values of any parameters except e and μ . The resulting sample of merging galaxies, shown in Figure 2, possess a variety of morphologies; only a subset display the “double tails” characteristic of the best known mergers (Toomre 1977).

3.2. Identikit Matching

We prepared a series of eight Identikit simulations spanning a range of pericentric separations. Each simulation contained two identical ($\mu = 1$) configurations of $N_{\text{test}} = 262,144$ test particles and $N_{\text{sphr}} = 81,920$ massive particles; the mass model used to set up the massive particle distribution was a spherical version of the one used in the random mergers. These configurations were placed on parabolic ($e = 1$) relative orbits with pericentric separations $p = 1/16, 2/16, 3/16, 4/16, 5/16, 6/16, 7/16$, and $8/16$, starting at $t = -2$ time units before the first pericenter, and followed until $t = 8$, by which time even the widest passage had merged.

We used these simulations and the Identikit software to fit each of the random mergers by interactively matching the

“observed” (X, Y) , (X, V) , and (V, Y) projections with test particles. The modeling process usually began with rough guesses for the viewing direction, time since pericenter, and pericentric separation. A variety of clues guided these guesses. For example, short but pronounced tidal features point to a recent tidal encounter, while long but attenuated features suggest an older passage; in later stages, loops associated with tails show that the material has started falling back. Likewise, if the galaxies display a large separation in projected velocity then the sight line must be close to the orbital plane; conversely, a small difference in projected velocity implies either that the system is observed near apocenter or that the relative velocity vector is roughly perpendicular to the line of sight. Finally, other things being equal, closer passages generally yield stronger and more dramatic tidal features.

The next step was to adjust the orientations of the two disks, attempting to roughly match the morphology and kinematics of the system. This generally suggested further modifications to the viewing direction, separation, and time, as well as the scale factors and center-of-mass position and velocity. Further adjustment of all parameters continued until a satisfactory match was obtained or exhaustion set in. Our criteria for a satisfactory match were somewhat subjective⁷; we placed a good deal of weight on matching tidal features (e.g., Figure 1), while recognizing that test particles cannot accurately reproduce structures—such as tidally induced spirals—that depend on self-gravity. Each match typically took a few hours, and the entire set of 36 random mergers was matched in about one month; for comparison, a match to the NGC 7252 merger remnant (Hibbard & Mihos 1995) took 74 N -body runs over a three month time period, while a match to the NGC 4676 system (Barnes 2004) took ~ 30 runs over two months.

After changing the viewing direction, time since pericenter, or orbital parameters, it is usually necessary to reposition the centers of the models on top of the actual positions by adjusting the rotation about the viewing axis θ_z , scale factor \mathcal{L} , and center-of-mass position $(X_{\text{cm}}, Y_{\text{cm}})$. We therefore implemented an option to “lock” the centers; when this option is invoked, θ_z , \mathcal{L} , and $(X_{\text{cm}}, Y_{\text{cm}})$ are recalculated on the fly, keeping the projected positions of the models invariant as other parameters are changed. Locking works quite well when the two galaxies are well separated on the (X, Y) plane; it is less useful, and can be downright counterproductive, when the centers appear close together. In fine tuning a nearly final match we sometimes found it useful to unlock the centers, trading off slight misalignments in central positions for improved matches to tidal features.

Figure 1, which shows our match to object 23 (see Figure 2), illustrates many aspects of the matching process. From the start, it seemed likely that the viewing direction would be fairly close to the orbital plane, since the two galaxies have rather different systemic velocities. The galaxy on the lower right of the (X, Y) projection appears nearly edge-on, as indicated by its morphology and its rather large velocity range. Since its tidal features lie more or less in the same plane as the disk itself, it seemed plausible that this galaxy has a relatively small inclination i_1 to the orbital plane, while its companion clearly has a higher inclination i_2 and appears more face-on from our viewpoint. The dual-valued velocities along the tail of the edge-on disk, which produce the hook-shaped feature seen in the (X, V) and (V, Y) projections, suggested that this tail is actually quite extended, but viewed so as to double back on itself.

⁷ It is not trivial to evaluate matches quantitatively; for more on this, see Section 4.2.1.

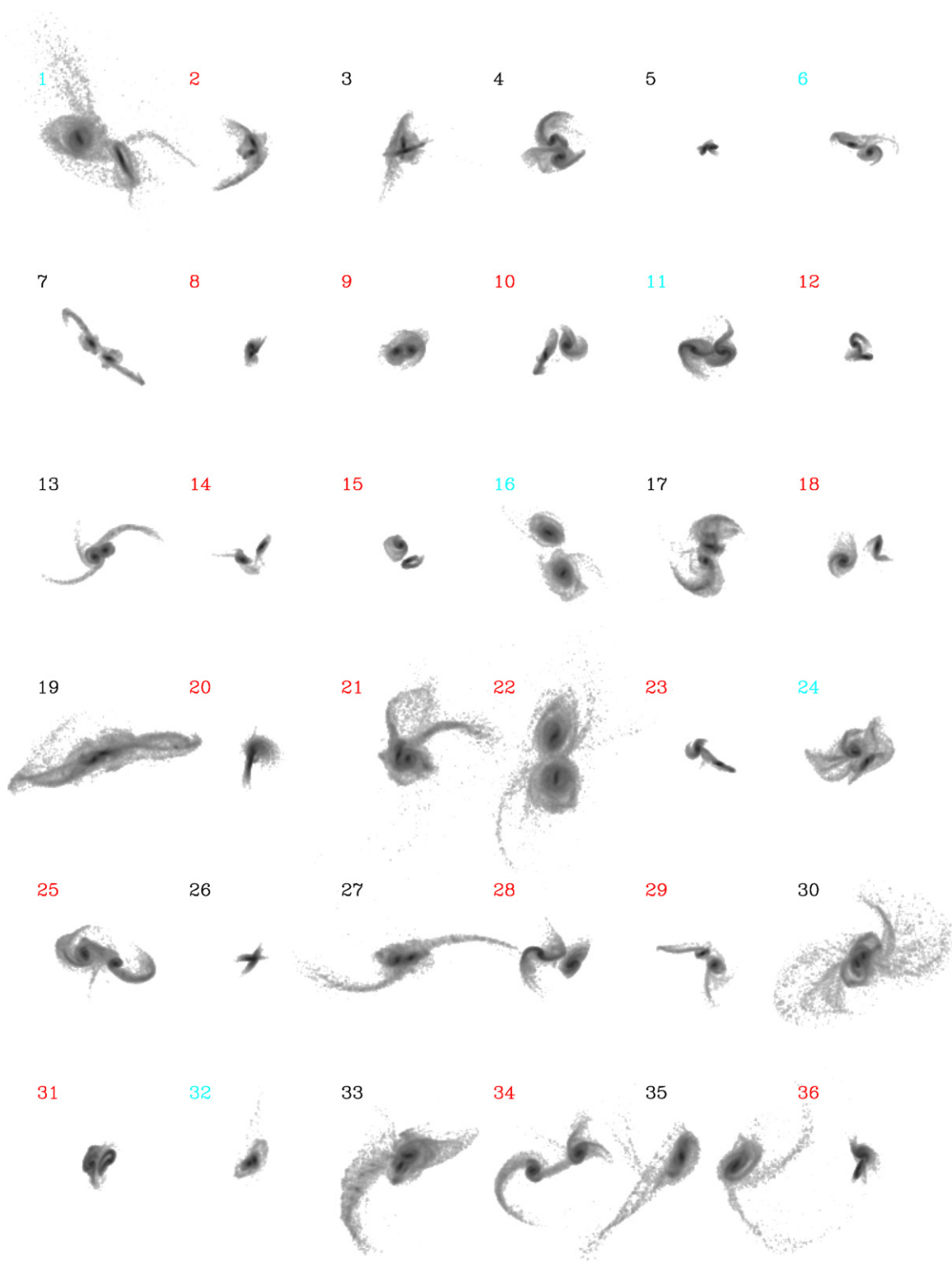


Figure 2. Sky-plane (X, Y) projections of the 36 merging encounters used to test the Identikit procedure. Note the range of sizes and morphologies. The number of each system appears to its upper left; color indicates the Identikit fit quality (see Section 3.2), with good fits in red, fair fits in black, and poor fits in blue. (A color version of this figure is available in the online journal.)

For an initial match to this system, we tried a “middle-of-the-road” pericentric separation ($p = 0.25$); at a relatively early time ($t = 0.56$) we could roughly match the velocity difference and some aspects of the morphology and kinematics, including the spiral morphology of the face-on disk and the hooked tail in the (V, Y) projection. However, other features of this initial match were less satisfactory. In the (X, V) projection, the tail doubled

back too soon, while in the (V, Y) projection, the bridge did not span the velocity range between the galaxies, falling to the left of its ideal position. Moreover, the more face-on disk, while nicely rendered in the (X, Y) projection, populated regions of phase space which the (V, Y) projection showed to be empty. Trial and error revealed that wider passages and later times could repair most of these defects; the solution shown in Figure 1 uses

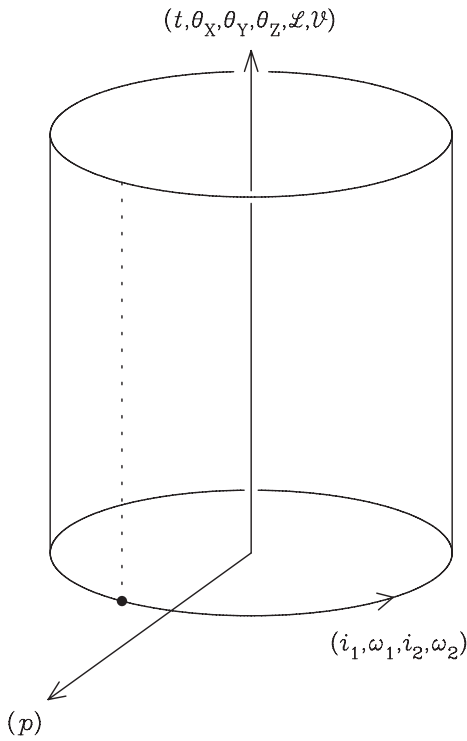


Figure 3. An abstract representation of the parameter space of galaxy interactions. The radial coordinate represents the initial orbit, the azimuthal coordinate represents the disk orientations, and the vertical coordinate represents the parameters chosen after a simulation is run. A conventional N -body simulation explores the parameter subspace represented by the dotted line, while a single Identikit simulation can explore the entire cylindrical surface.

a $p = 0.5$ passage viewed at $t = 1$. The tail in this match, while more extended than it was initially, is still a bit too short. Times $t > 1$ yield longer tails, but the velocity difference between the galaxies becomes too small, and bridge particles falling through the more face-on disk overpopulate a relatively sparse region of phase space. The adopted solution is therefore a compromise between several competing factors.

After comparing our Identikit models to the morphology and kinematics of all 36 random mergers, we subjectively graded the solutions as “good” (18 cases), “fair” (12 cases), or “poor” (6 cases); these grades are indicated in Figure 2. Good matches, such as those in Figure 1, strongly constrain the parameters. Fair matches generally appear plausible but allow more latitude in selecting parameter values; this group included several systems with twin edge-on tidal tails. Poor matches could be divided into two groups: systems with weak and diffuse tidal features, typically resulting from very wide encounters involving retrograde or highly inclined galaxies (objects 16 and 32), and systems with pronounced but confusing tidal features (objects 1, 6, 11, and 24).

3.3. Results: Parameters

With the Identikit solutions in hand, we compared their parameter values to the true values used to generate the artificial merger data. Figure 3 uses an abstract cylindrical coordinate system to portray the parameter space explored in these solutions. The radial coordinate represents the initial orbit of the two galaxies; the fits discussed here parameterize the orbit by the pericentric separation p , since the eccentricity e and mass ratio μ were fixed beforehand. The azimuthal coordinate represents the four angles, (i_1, ω_1) and (i_2, ω_2) , required to specify the initial orientations of the two disks. Together, the radial

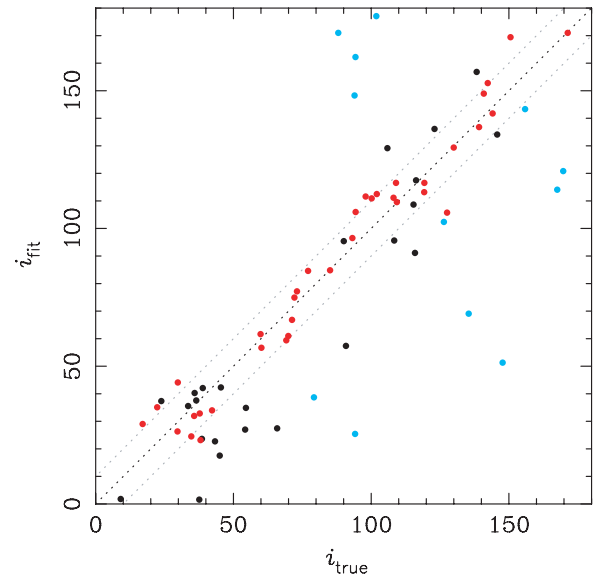


Figure 4. Estimates of disk inclination, i . The color of each data point shows the quality of the fit: red is good, black is fair, and blue is poor. The heavy dotted line represents perfect agreement ($i_{\text{fit}} = i_{\text{true}}$); the light lines show $i_{\text{fit}} = i_{\text{true}} \pm 10^\circ$. (A color version of this figure is available in the online journal.)

and azimuthal coordinates of this abstract space completely specify the initial conditions for a galaxy interaction. The vertical coordinate represents the parameters selected *after* running a simulation: time since pericenter t , viewing angles $(\theta_X, \theta_Y, \theta_Z)$, and scale factors $(\mathcal{L}, \mathcal{V})$; here the center-of-mass parameters are omitted since their values are not discussed below. A conventional N -body simulation starts at a point on the horizontal plane and explores the parameter subspace represented by the dotted line in this figure; a single Identikit simulation, in contrast, allows access to an entire cylindrical surface.

Figure 4 presents a scatter plot comparing inclinations i_{fit} derived from the Identikit fits against the inclinations i_{true} used in the random merger sample. Here and in subsequent plots, color indicates the grade of each model; note that the disks are not graded individually, so both disks in a given model receive the same grade even if one fits better than the other. The good fits (shown in red) fall quite close to the diagonal line across the entire range of the plot. The fair fits (black) display more scatter but track the same relationship. In contrast, the poor fits (blue) have a very different distribution: almost all have inclinations $i_{\text{true}} > 90^\circ$, and most fall quite far from the diagonal. This plot supports a couple of useful inferences. First, our subjective grades, based on the overall appearance of the Identikit models, correlate with $|i_{\text{fit}} - i_{\text{true}}|$; in other words, these grades mean something. Second, encounters involving disks with inclinations $i > 90^\circ$ are more difficult to model, presumably because the tidal features such encounters produce are less distinct and more ambiguous. Nonetheless, many high-inclination encounters were successfully modeled; other factors evidently influence the outcome of the modeling process.

Likewise, Figure 5 compares fit and true values of the argument to pericenter, ω_{fit} and ω_{true} . Since ω becomes indeterminate for inclinations near $i = 0^\circ$ or $i = 180^\circ$, we plot disks with $30^\circ \leq i_{\text{true}} \leq 150^\circ$ as filled circles, and disks outside this range as crosses. This plot shows that good fits yield arguments quite close to the true values, and the fair fits do nearly as well. At first sight it may seem that a few disks, represented by the one good and three fair points in the upper left and lower right of the plot, yield discrepant values of ω_{fit} , but this is an

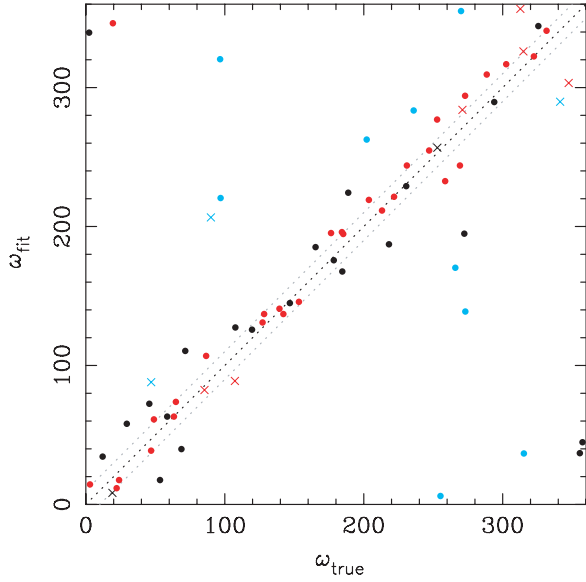


Figure 5. Estimates of disk argument, ω . Colors and dotted lines as in Figure 4; crosses represent disks with $|i_{\text{true}} - 90^\circ| > 60^\circ$. Note that opposing edges of this plot should be identified.

(A color version of this figure is available in the online journal.)

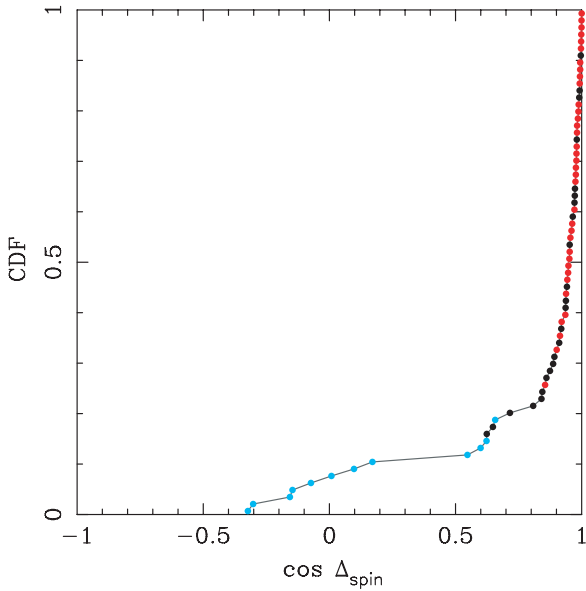


Figure 6. Cumulative distribution function for $\cos(\Delta_{\text{spin}})$. Color shows the fit quality.

(A color version of this figure is available in the online journal.)

artifact of topology; ω is a periodic coordinate, and when opposing edges of the plot are identified, these apparent outliers are not so far from $\omega_{\text{fit}} = \omega_{\text{true}}$. The poor fits, in contrast, genuinely scatter throughout the plot. Most of the good and fair fits with $i_{\text{true}} < 30^\circ$ or $150^\circ < i_{\text{true}} < i_{\text{true}}$ still yield reasonable values for ω , but these are a bit more scattered. For example, only one of the six good fits with i_{true} in this range yields a ω_{fit} within 10° of ω_{true} ; in contrast, just over half of the good fits with inclinations $30^\circ \leq i_{\text{true}} \leq 150^\circ$ have $|\omega_{\text{fit}} - \omega_{\text{true}}| < 10^\circ$.

To examine our overall accuracy in determining initial disk orientations, we computed misalignments Δ_{spin} between true and fitted spin vectors for all 72 disks. Figure 6 shows the cumulative distribution function of $\cos(\Delta_{\text{spin}}) = \hat{\mathbf{s}}_{\text{fit}} \cdot \hat{\mathbf{s}}_{\text{true}}$; as in previous plots, color indicates the subjective grade of each fit. A

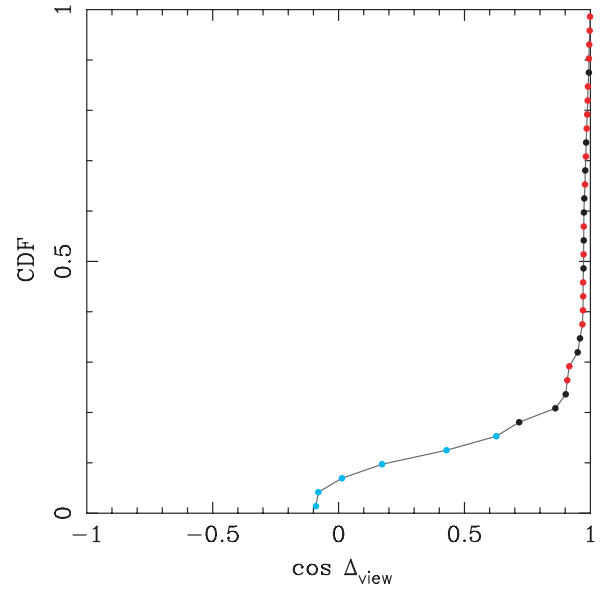


Figure 7. Cumulative distribution function for $\cos(\Delta_{\text{view}})$. Color shows the fit quality.

(A color version of this figure is available in the online journal.)

perfect match yields $\cos(\Delta_{\text{spin}}) = 1$, while if $\hat{\mathbf{s}}_{\text{fit}}$ was uncorrelated with $\hat{\mathbf{s}}_{\text{true}}$ then $\cos(\Delta_{\text{spin}})$ would be uniformly distributed in the range $[-1, 1]$ and the plotted points would fall along a diagonal from lower left to upper right. The actual distribution is strongly peaked near $\cos(\Delta_{\text{spin}}) = 1$, with the good fits showing the smallest misalignments, the poor fits showing the largest misalignments, and the fair fits falling in between. This is consistent with the previous figures, since i and ω are just angular coordinates for $\hat{\mathbf{s}}$. For the entire sample, the median value is $\Delta_{\text{spin}} = 18^\circ$, while for the 36 disks in good fits the median is $\Delta_{\text{spin}} = 12^\circ$.

In a similar fashion, Figure 7 shows the distribution of the misalignment in the viewing direction, Δ_{view} , for all 36 fits. Here $\cos(\Delta_{\text{view}}) = \hat{\mathbf{z}}_{\text{fit}} \cdot \hat{\mathbf{z}}_{\text{true}}$, perfect agreement again yields $\cos(\Delta_{\text{view}}) = 1$, and perfect ignorance would distribute points along a diagonal from lower left to upper right. The viewing direction is quite well determined; for the entire sample the median $\Delta_{\text{view}} = 13^\circ$, while for the 18 good fits alone the median is only slightly smaller, $\Delta_{\text{view}} = 12^\circ$. Note that an error circle with a radius of 12° covers roughly 1% of the solid angle of a sphere; these fits are *much* better than educated guesses.

Figure 8 compares the actual time t_{true} since pericenter against the time t_{fit} obtained from the Identikit fit. The scatter plot on the left shows that the fitted and true values are in good agreement, closely tracking each other throughout the entire range of times; there is no evidence of bias or systematic error, and the residuals appear to be random. The plot on the right shows the cumulative distribution of the fit/true ratio, $t_{\text{fit}}/t_{\text{true}}$. The symmetric appearance of this curve provides further evidence that t is accurately estimated by the Identikit models. Subjective fit quality appears to correlate with $t_{\text{fit}}/t_{\text{true}}$; of the ten points at the two extremes of the distribution, only one comes from a good fit.

Figure 9 compares fitted and true values of the pericentric separation. Here the range of p values is rather small, and the fact that p_{fit} can take on only eight discrete values is evident. There is a fair correlation between p_{fit} and p_{true} , although the points show considerable scatter. The cumulative

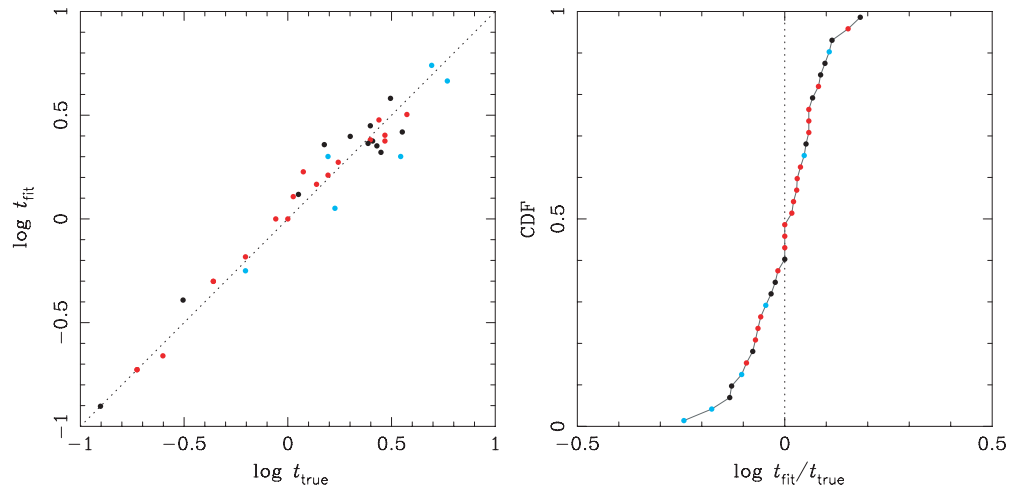


Figure 8. Estimates of the dimensionless time since pericenter, t . Left: scatter plot of $\log t_{\text{fit}}$ against $\log t_{\text{true}}$. Right: cumulative distribution function of $\log t_{\text{fit}}/t_{\text{true}}$. In both plots, color shows the fit quality, and the dotted line represents perfect agreement ($t_{\text{fit}} = t_{\text{true}}$). (A color version of this figure is available in the online journal.)

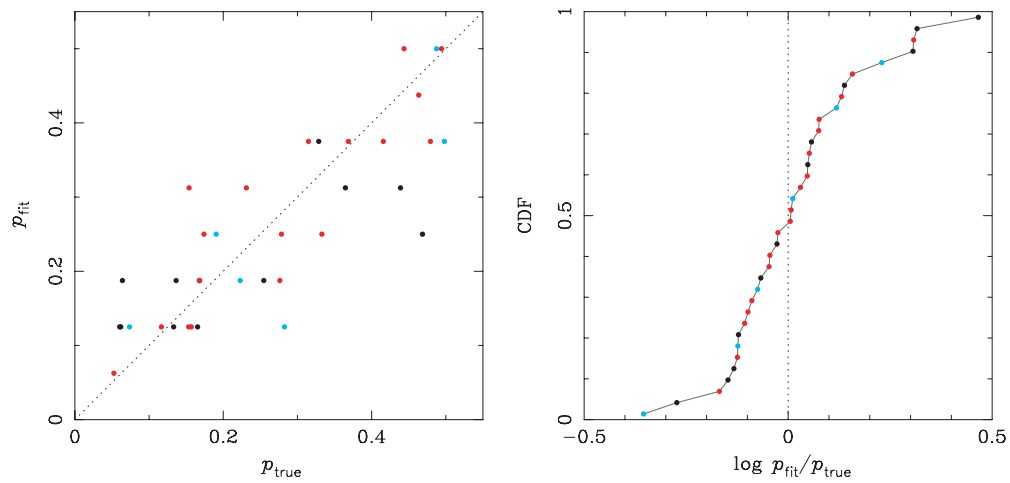


Figure 9. Estimates of the dimensionless pericentric separation, p . Left: scatter plot of p_{fit} against p_{true} . Right: cumulative distribution function of $p_{\text{fit}}/p_{\text{true}}$. Colors and dotted lines as in Figure 8. (A color version of this figure is available in the online journal.)

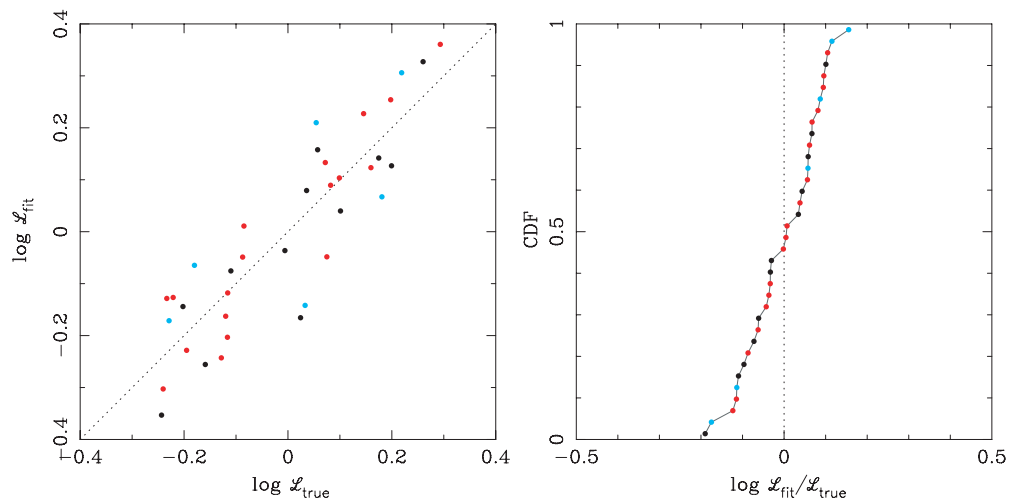


Figure 10. Estimates of the length scale factor, \mathcal{L} . Left: scatter plot of $\log \mathcal{L}_{\text{fit}}$ against $\log \mathcal{L}_{\text{true}}$. Right: cumulative distribution function of $\mathcal{L}_{\text{fit}}/\mathcal{L}_{\text{true}}$. Colors and dotted lines as in Figure 8. (A color version of this figure is available in the online journal.)

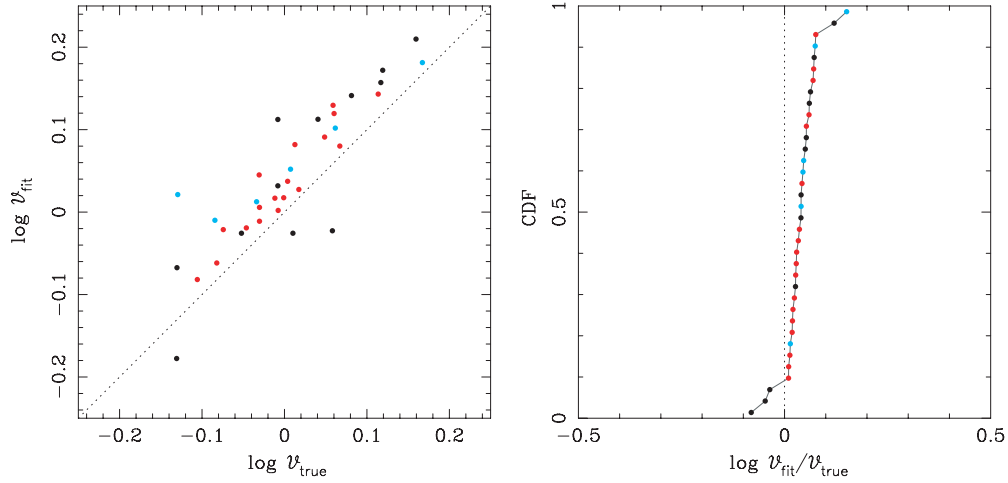


Figure 11. Estimates of the velocity scale factor, \mathcal{V} . Left: scatter plot of $\log \mathcal{V}_{\text{fit}}$ against $\log \mathcal{V}_{\text{true}}$. Right: cumulative distribution function of $\mathcal{V}_{\text{fit}}/\mathcal{V}_{\text{true}}$. Colors and dotted lines as in Figure 8.

(A color version of this figure is available in the online journal.)

Table 1
Ratios of Fit/True Parameter Values for all 36 Models

Parameter		1 st Quart	Median	3 rd Quart
Time since pericenter	t	0.86	1.02	1.14
Pericentric separation	p	0.79	1.01	1.25
Length scale factor	\mathcal{L}	0.86	1.01	1.17
Velocity scale factor	\mathcal{V}	1.05	1.10	1.15
Physical time	T	0.78	0.95	1.02
Physical separation	P	0.87	0.97	1.13

distribution of $p_{\text{fit}}/p_{\text{true}}$ plotted on the right is nonetheless fairly symmetric, and the median value of $p_{\text{fit}}/p_{\text{true}}$ is very close to unity. Curiously, there is not much sign that the grades assigned the models correlate with $p_{\text{fit}}/p_{\text{true}}$; fair and poor fits appear interspersed with good ones throughout most of the distribution.

Identikit estimates of the length and velocity scale factors, \mathcal{L} and \mathcal{V} , are compared with their true values in Figures 10 and 11, respectively. The length scale \mathcal{L} is well determined; the plot on the left shows points scattered about the diagonal line, while the cumulative distribution on the right shows a narrow spread with a median value of $\mathcal{L}_{\text{fit}}/\mathcal{L}_{\text{true}}$ close to unity. In contrast, Identikit estimates of the velocity scale \mathcal{V} show a small but very definite bias; the distribution of $\mathcal{V}_{\text{fit}}/\mathcal{V}_{\text{true}}$ is narrow, but clearly offset from unity. Tests with isolated disks suggest that the absence of random motion in the Identikit test-particle disks is responsible (see Appendix C).

Table 1 lists statistics for the ratios of fitted to true values for t , p , \mathcal{L} , and \mathcal{V} ; the physical parameters T and P will be discussed in the next section. Fit/true ratios for t and \mathcal{L} have fairly narrow distributions centered on unity, confirming that these parameters are determined accurately and without bias. The fit/true distribution for p , while somewhat broader, is also centered on unity. The fit/true distribution for the velocity scale factor \mathcal{V} is quite narrow, but the median value is $\sim 10\%$ too high, showing again that a small bias is present in fitting \mathcal{V} .

3.4. Results: Residuals

The errors determined by comparing the Identikit models with the actual mergers define six independent residuals: viewing direction (Δ_{view}), spin direction (Δ_{spin}), time since

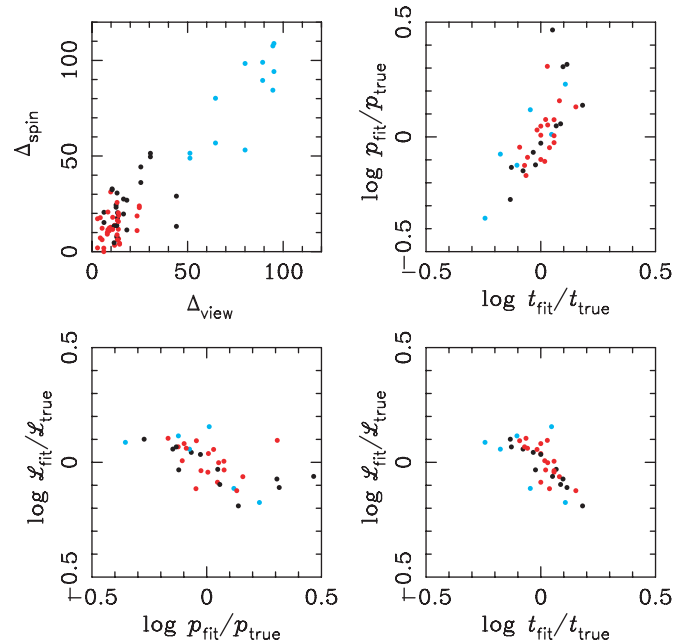


Figure 12. Scatter plots of statistically significant correlations between residuals in Identikit models. Color indicates the quality of fit. The plot on the upper left contains twice as many points as the others because Δ_{spin} is plotted for each disk.

(A color version of this figure is available in the online journal.)

pericenter ($t_{\text{fit}}/t_{\text{true}}$), separation at pericenter ($p_{\text{fit}}/p_{\text{true}}$), length scale ($\mathcal{L}_{\text{fit}}/\mathcal{L}_{\text{true}}$), and velocity scale ($\mathcal{V}_{\text{fit}}/\mathcal{V}_{\text{true}}$). If each of these residuals is plotted against the others, a total of 15 ($6 \times 5/2$) potential relationships can be examined. Most of these plots show no measurable correlation; only the four in Figure 12 are significant (correlation coefficient > 0.5).

As shown in the upper left panel of Figure 12, errors in disk orientation Δ_{spin} are correlated with errors in viewing direction Δ_{view} . This correlation, which is largely driven by the poor fits, is not hard to explain. Once a viewing direction has been selected, the next step is usually to adjust the disk orientations; if clear guidance from tidal features is lacking, the best one can do is to match each disk's position angle and apparent tilt with respect to the line of sight. A poor choice for the viewing direction will induce comparable errors in spin direction, as seen here.

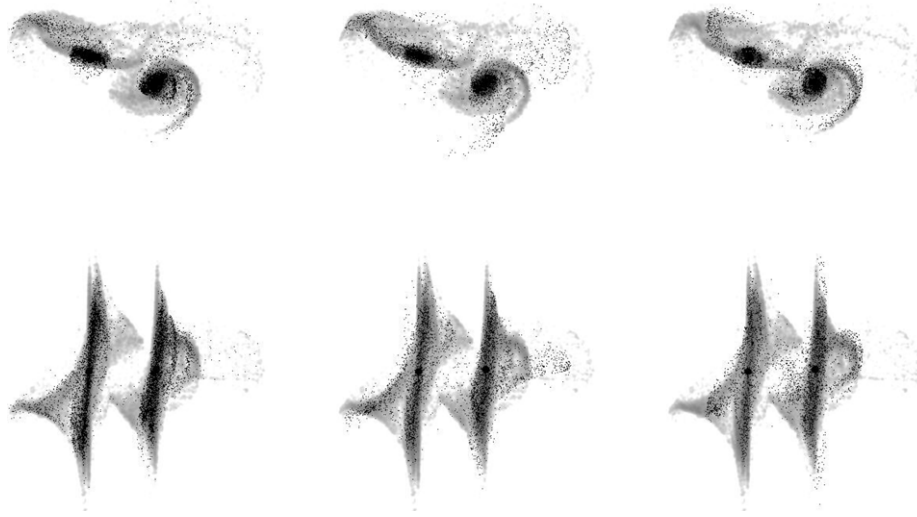


Figure 13. Three models in search of a match. Gray-scale images show the “observed” data (object 6 in Figure 2), while points represent models. Top and bottom rows show projections on (X, Y) and (X, V) planes, respectively. Left: the “correct” Identikit solution. Middle: a match to the shape and velocities of the more edge-on disk. Right: a match to the spiral features of the more face-on disk.

The plot in the upper right panel shows that residuals in the time since pericenter t correlate with residuals in pericentric separation p . This correlation also has a simple explanation; wider passages evolve and merge more slowly, so if t_{fit} is for some reason overestimated during the matching process then a larger p_{fit} can partly compensate for this error. As an extreme example, suppose t_{fit} was set so high that an encounter with the correct p_{fit} would already have merged by this time; by selecting a larger value for p_{fit} , the merger can be delayed until some time after t_{fit} , improving the match to the morphology.

A clear correlation between the residuals in t and \mathcal{L} of the form $\mathcal{L}_{\text{fit}}/\mathcal{L}_{\text{true}} \simeq (t_{\text{fit}}/t_{\text{true}})^{-1}$ is shown in the lower right panel of Figure 12. Such a correlation arises naturally in cases where fits are strongly constrained by well-developed tidal tails. In a proper tail, material at the tip moves fast enough to escape; at late times this material will asymptotically have a constant velocity (Toomre & Toomre 1972), implying that a tail’s length grows in proportion to its age (Schweizer 1977). If t_{fit} is overestimated, tidal tails will be longer in direct proportion, and a smaller value of \mathcal{L}_{fit} will be needed to rescale them to their correct physical lengths. It is likely that similar considerations also apply when other kinds of tidal features provide the primary constraints; this is consistent with the results presented here, which show that the good and fair fits fall close to $\mathcal{L}_{\text{fit}}/\mathcal{L}_{\text{true}} \simeq (t_{\text{fit}}/t_{\text{true}})^{-1}$, while the poor ones are more scattered.

Finally, we conjecture that the correlation between residuals of p and \mathcal{L} shown in the lower left panel is induced by the $t_{\text{fit}}/t_{\text{true}} - p_{\text{fit}}/p_{\text{true}}$ and $t_{\text{fit}}/t_{\text{true}} - \mathcal{L}_{\text{fit}}/\mathcal{L}_{\text{true}}$ correlations already described. Of the three, the $p_{\text{fit}}/p_{\text{true}} - \mathcal{L}_{\text{fit}}/\mathcal{L}_{\text{true}}$ correlation shows the most scatter, and its outliers tend to match those in the $t_{\text{fit}}/t_{\text{true}} - p_{\text{fit}}/p_{\text{true}}$ correlation.

An interesting consequence of these correlations emerges when the dimensionless model parameters t and p are combined with the length and velocity scale factors \mathcal{L} and \mathcal{V} . In matching an Identikit model to observational data, X and Y might be given in units of kpc, and V might be given in units of km s^{-1} ; the scale factors \mathcal{L} and \mathcal{V} would then have units of kpc and km s^{-1} , respectively, and define a transformation from dimensionless model data to real physical values. The physical pericentric separation is $P = \mathcal{L}p$, while the time since pericenter is $T = (\mathcal{L}/\mathcal{V})t$. A glance at the two lower plots in Figure 12 suggests that these correlations may actually *reduce* errors in

estimates of the physical parameters T and P . Table 1 supports this; the uncertainty in P , as indicated by the ratio of third to first quartile values, is about half the uncertainty in p . For T the improvement is not as striking; the ratio of third to first quartiles is slightly smaller than the ratio for t , but it appears that \mathcal{V} introduces some additional scatter and a small bias.

3.5. Poor Matches

For balance, it is worth taking a closer look at some of the less successful matches. We judged six out of 36 of our solutions to be poor fits to the “observed” data. As already noted, two of the systems with poor matches had very diffuse tidal features, while four had fairly strong features. Our difficulties in modeling the latter are somewhat surprising; why, given the information which must be present in strong tidal features, did not the models not turn out better?

Figure 13 presents three versions of one of the more difficult systems (object 6 in Figure 2). For ease of comparison, only the (X, Y) and (X, V) planes are shown; the (V, Y) views are harder to interpret since the galaxies partly overlap. The left-hand version shows an Identikit model with the correct disk orientations, viewing direction, and velocity scale “dialed in” by hand. Only a finite set of pericentric separations are available in Identikit, so it was not possible to exactly match the pericentric separation $p_{\text{true}} = 0.223$; on the whole, $p_{\text{fit}} = 3/16$ gave a better match than $p_{\text{fit}} = 1/4$ although the latter is numerically closer. This closer approach favored a somewhat different length scale ($\mathcal{L}_{\text{fit}} = 0.644$ versus $\mathcal{L}_{\text{true}} = 0.590$) and a slightly earlier time ($t_{\text{fit}} = 1.62$ versus $t_{\text{true}} = 1.69$); both of these adjustments are qualitatively consistent with the residual correlations discussed in the last section.

The “correct” solution on the left in Figure 13 does a poor job of matching the morphology (top). It does better at matching the kinematics (bottom), although some fairly large regions of phase space are quite underpopulated, and one of the spiral arms in the more face-on disk produces a badly placed streak of particles across the (X, V) projection. By our subjective criteria, this solution is a poor fit. Since the disk orientations and viewing direction *exactly* match those used to generate the gray-scale images, this mismatch must be largely due to the lack of disk self-gravity in the Identikit simulations. In particular, the spiral

morphology of the more face-on disk is very poorly reproduced; with hindsight, we recognize that this spiral probably owes its form to self-gravity.

The middle and right parts of Figure 13 present two of the solutions that we found while trying to match this system. Essentially, each matches one galaxy while failing to match the other. The middle solution does a plausible job of matching the morphology *and* kinematics of the more edge-on disk, using a close passage ($p_{\text{fit}} = 1/16$) at an early time ($t_{\text{fit}} = 1.12$). Although it does a very poor job with the more face-on disk, this solution is actually not too bad—the viewing angle is off by 47° , but the disks are within 30° of their correct orientations. The right-hand solution approximates the morphology and kinematics of the more face-on disk, using a wider passage ($p_{\text{fit}} = 3/16$) at the same early time. Ironically, although the decent-looking fit to the face-on disk and somewhat plausible match to the edge-on disk led us to adopt this solution as the best of a bad lot, it is actually a *much* less accurate fit than the middle one—the viewing angle is off by 95° , while the face-on and edge-on disks are misaligned by 109° and 94° , respectively. The splattering of particles between the galaxies in the (X, V) projection, populating a region which should have been completely empty, was the critical flaw which saved us from assigning a “fair” grade to this solution.

The other three systems which we failed to fit despite their strong tidal features are a mixed lot. In object 24, much as in the example just discussed, the “correct” Identikit solution does not match the morphology of either galaxy. In object 11, the correct solution matches one disk but fails to reproduce the morphology and kinematics of its partner. Finally, object 1 is reproduced quite accurately by the correct Identikit model. Our failure with object 1 was largely due to insufficient patience, while with object 24 the mismatch was so bad that the correct solution does not stand out when compared with other possible fits. Object 11 is intermediate; had we stumbled across the correct match to one disk we might have recognized the overall plausibility of this solution. In sum, human limitations and lack of self-gravity contribute about equally to the four poor matches of systems with strong tidal features.

4. DISCUSSION

Under somewhat idealized conditions, the Identikit methodology can recover the key parameters of a galactic encounter from a single data cube. If the method can also be applied to real data, it will be a powerful tool for interpreting observations and reconstructing the dynamical histories of interacting galaxies. But before going further, some limitations should be discussed.

4.1. Limitations

First, as noted above, Identikit simulations are not completely self-consistent. Halos and bulges are treated self-consistently, but disks—of necessity—must be modeled with test particles. Disk structures requiring self-gravity, including bars and swing-amplified spirals, will not be reproduced. Consequently, these features cannot be used to match models to observations. Moreover, orbital decay of Identikit models is independent of disk orientation, whereas direct passages are expected to decay faster than the retrograde ones (White 1979; Barnes 1992). For a pair of galaxies approaching their second passage, the estimated time t_{fit} since first pericenter may be off by as much as $\sim 20\%$; in applications requiring an accurate estimate of t_{fit} ,

Identikit models should be followed up with self-consistent simulations.

Second, while the test particles we used to model disks are collisionless, most kinematic tracers follow a specific phase of the interstellar medium—for example, H I, H α , or CO. Collisionless particles can approximate gas dynamics, but only if the gas moves ballistically; streams of particles freely interpenetrate, whereas gas will be deflected if it encounters shocks. Examples include mass transfer via genuine bridges formed in low-inclination encounters (Toomre & Toomre 1972) and “splash bridges” due to hydrodynamic forces in interpenetrating encounters (Struck 1997). More subtle are the modest star–gas offsets seen in low-inclination encounters with extended gas disks (Mihos 2001); it appears that the gas offset from the stars does follow ballistic trajectories, while some gas initially associated with the stars dissipates and falls back. Additionally, shocks may change the physical state of the gas; in particular, dense molecular gas is often associated with material which has undergone significant dissipation and hence *cannot* be modeled collisionlessly. But for most encounter geometries, gas in tidal features should be well approximated by collisionless particles; exceptions can be recognized and allowed for in the fitting process. Stars, especially populations predating the onset of an encounter, could be a useful complement to gas-phase tracers; absorption-line spectroscopy would require prohibitively large amounts of telescope time, but individual planetary nebulae are already providing kinematic data for nearby systems (e.g., Hui et al. 1995; Durrell et al. 2003).

Third, two parameters were not included in the present experiment: the orbital eccentricity e and the mass ratio μ . In principle, it is straightforward to include these parameters in the fitting process, although doing so increases the number of Identikit models needed. Both parameters have a priori constraints—orbits with $e \sim 1$ are favored theoretically (Toomre & Toomre 1972; but see Khochfar & Burkert 2006), while μ can sometimes be estimated photometrically assuming constant M/L ratios—so it seemed reasonable to exclude them from the initial experiments. Putting these parameters in play would probably increase the scatter in our fits; moreover, the three-way correlation between residuals of t , p , and \mathcal{L} (Section 3.4) might expand to involve residuals of e and μ as well. Within the context of the models examined here, there is scant reason to expect much cross-talk between these parameters and others; in particular, disk orientations and viewing angles are robustly constrained by tidal features and should be well determined even if e and μ are included in the fits.

Fourth, real galaxies have a range of rotation curve shapes, reflecting a diversity of mass profiles (e.g., Casertano & van Gorkom 1991; Catinella et al. 2006); a single mass model is too limited. The fact that we used the same mass model for our artificial data *and* for the Identikit simulations no doubt helped to reduce the uncertainties in our solutions. There is no reason why Identikit simulations cannot include a variety of mass models, although this will increase the number of choices to be made in modeling a galactic collision. On the other hand, if such simulations can discriminate between different mass models then they would provide a way to analyze the structure of disk galaxies.

4.2. Previous Studies

Models of interacting galaxies have a long history. Toomre & Toomre (1972) presented test-particle models of four systems: Arp 295, M 51, NGC 4676, and NGC 4038/9. The latter three have been revisited time and again by other workers. Kinematic

information was initially scarce and of uneven quality, so early modeling attempts focused on reproducing the optical morphology. Better velocity data have given kinematics a more substantial role in more recent modeling efforts. At the same time, faster computers and N -body algorithms have enabled researchers to construct models incorporating self-gravity.

The methodology adopted by Hibbard & Mihos (1995) in their model of the well known merger remnant NGC 7252 includes several key practices found in other successful models.

1. Detailed velocity information, in the form of H I data (Hibbard et al. 1994), was available to constrain the model.
2. Astrophysical arguments were used to estimate several critical parameters—specifically, the mass ratio μ , the initial orbital eccentricity e , and the pericentric separation p .
3. The model focused on reproducing the large scale, and morphology and kinematics of the tidal tails; these features evolved ballistically since first passage and therefore carry a memory of the initial encounter.
4. Test-particle models, with rigid galaxy potentials constrained to follow realistic merger trajectories, were used to narrow down the range of parameter space.
5. Fully self-consistent N -body models were used to refine the final model.
6. Simulation particles were plotted over orthogonal projections of the data cube to show that the final model reproduced *both* the morphology and the kinematics of NGC 7252.

Table 2 lists some interacting disk galaxies with dynamical models incorporating significant kinematical constraints. The progenitors of these systems span a range of mass ratios and morphological types. “S+S” systems involve two disk galaxies of roughly comparable mass, both generally displaying significant tidal features. Most of these pairs are observed between first and second passages; NGC 7252 is the only completed merger. As Struck et al. (2005) note in modeling NGC 2207, earlier stages are generally easier to fit. In “S+d” encounters a disk galaxy is perturbed by a smaller companion, while in “E+S” systems the disk is disturbed by an elliptical comparable mass. Finally, in “ring” galaxies a companion has plunged almost perpendicularly through a disk galaxy (Appleton & Struck-Marcell 1996); these systems are relatively straightforward to model since their geometry is fairly simple.

To varying degrees, the studies in Table 2 all followed the methodology used by Hibbard & Mihos (1995). Most had access to detailed velocity information, usually obtained by H I interferometry or H α Fabry–Perot imaging, although a few models were based on long-slit spectroscopy. Adopted orbital eccentricities reflect a range of assumptions, not all equally plausible; for most systems, orbits with $e \sim 1$ seem more likely since $e < 1$ begs the question of what happened on the *previous* passage. Both test-particle and self-consistent techniques were used. Not all models were refined using fully self-consistent simulations; inasmuch as orbital decay is critical for many of these systems, the use of rigid potentials may be problematic in some cases.

As the third column of Table 2 shows, a wide range of criteria were used to define an acceptable match to the observations. Many studies still seemed more focused on morphology than kinematics, and less than half presented compelling quantitative comparisons between models and data. Matches labeled “kin2” used two-dimensional kinematical information, and presented

the models and data in such a way that direct and unambiguous comparisons could easily be made—ideally, the model and data were overplotted, or at a minimum plotted to the same scale and orientation. Matches labeled “kin1” used one-dimensional data (e.g., long-slit spectra or mean velocities plotted as functions of a single coordinate), but again compared models and data directly. A few studies, labeled “gen” (for genetic), numerically evaluated matches; these will be discussed in Section 4.2.1. Most of the remaining studies, while drawing on spatially resolved kinematic information, presented essentially qualitative comparisons between models and data; these matches are labeled “qual” in the table. This designation is rather broad, ranging from studies which plotted models and data on different scales to studies which matched general kinematic trends or asserted, without providing quantitative evidence, that the model matched the data. Finally, a few studies which matched morphology only are designated “morph”; these are included when they served as precursors to more comprehensive modeling efforts.

The present study, while restricted to artificial data, closely parallels the approach of Hibbard & Mihos (1995). We depart from them in treating the pericentric separation p as a free parameter, and in not using fully self-consistent simulations to finalize the models. The latter, of course, is deliberate; one of our goals was to see if an approach combining test-particle disks with self-consistent halos can recover the encounter parameters of interacting disk galaxies. In practice, we envision using Identikit models to jump-start fully self-consistent simulations. We strongly concur that kinematic data provide an acid test which any dynamical model must pass (Toomre & Toomre 1972; Borne & Richstone 1991), and that large-scale tidal features are the key to unlocking the dynamical history of galactic encounters. Finally, we emphasize that direct and unambiguous comparison between the simulations and the “observational” data was a necessary ingredient of our approach. Overplotting the particles on the data, as in Figure 1, is an effective way to present such comparisons.

4.2.1. Genetic Algorithms

To date, most attempts to model interacting galaxies have relied on expert judgment in selecting initial conditions and identifying good matches between simulations and observations. Recognizing the considerable labor involved, several groups have tried to automate the modeling process (Wahde 1998; Theis & Kohle 2001; Gomez et al. 2002). The proposed algorithms have two essential components. First, they must replace the subjective comparison of the simulation particles (\mathcal{P}) and the observed data (\mathcal{D}) with an objective criterion $\mathcal{F}(\mathcal{P}, \mathcal{D})$ measuring the goodness of fit. Second, they must perform an efficient search of a very large parameter space. In view of the number of parameters involved, a blind search is impractical; these groups have adopted strategies mimicking biological evolution, generally known as *genetic algorithms* (Holland 1975).

Genetic algorithms create a population of N_{pop} individuals, each representing a possible solution to the problem at hand; in this case, an individual defines a set of initial conditions and viewing parameters. The evolutionary fitness of individual i is determined by using its initial conditions and viewing parameters to produce a particle distribution \mathcal{P}_i which is evaluated using $\mathcal{F}(\mathcal{P}_i, \mathcal{D})$. Once all N_{pop} individuals have been evaluated, the fittest among them are bred together to form a new generation, and the entire process is repeated. After N_{gen} generations, the population converges toward a nearly

Table 2
Dynamical Models of Interacting Disk Galaxies^a

System ^b	Arp	VV	Type	Match ^c	Reference
VV 784		784	ring	morph	Toomre (1978)
				kin1	Struck-Marcell & Higdon (1993)
VV 347, Arp 119	119	347	ring	qual	Hearn & Lamb (2001)
NGC 520	157	231	S+S	kin1	Stanford & Balcells (1991)
3C 48			S+S	kin1	Scharwächter et al. (2004)
NGC 672 / IC 1727		338	S+S	kin2	Combes et al. (1980)
NGC 1143/44	118	331	E+S	qual	Lamb et al. (1998)
IC 1908, AM 0313-545			S+d	qual	Mihos et al. (1993)
NGC 2207 / IC 2163			S+S	qual	Elmegreen et al. (1995)
				kin2	Struck et al. (2005)
VV 785, AM 0644-741		785	ring	kin1	Antunes & Wallin (2007)
NGC 2442 / AM 0738-692			S+d	qual	Mihos & Bothun (1997)
II Hz 4			ring	qual	Lynds & Toomre (1976)
NGC 2782	215		S+? ^d	qual	Smith (1994)
NGC 2992/93	245		S+S	kin2	Duc et al. (2000)
NGC 3031/77			S+d	qual	Thomasson & Donner (1993)
NGC 3031/34/77			S+S+d	qual	Brouillet et al. (1991)
				qual	Yun (1999)
AM 1003-435			S+S	qual	Günthardt et al. (2006)
NGC 3395/96	270	246	S+S	kin1	Clemens et al. (1999)
NGC 3448 / UGC 6016	205		S+d	qual	Noreau & Kronberg (1986)
NGC 4038/39	244	245	S+S	morph	Toomre & Toomre (1972)
				kin2	van der Hulst (1979)
				qual	Mahoney et al. (1987)
				qual	Barnes (1988)
				qual	Mihos et al. (1993)
				kin2	Hibbard (2003)
NGC 4254/92? ^e			S+S	qual	Duc & Bornaud (2008)
NGC 4435/38	120	188	S0+S	morph	Combes et al. (1988)
				kin2	Vollmer et al. (2005)
NGC 4449 / DDO 125			S+d	gen	Theis & Kohle (2001)
NGC 4654/39? ^e			S+S	kin2	Vollmer (2003)
NGC 4676	242	224	S+S	morph	Toomre & Toomre (1972)
				qual	Stockton (1974)
				kin1	Mihos et al. (1993)
				qual	Gilbert & Sellwood (1994)
				kin1	Sotnikova & Reshetnikov (1998)
				kin2	Barnes (2004)
NGC 5194/95	085	001	S+S0	morph	Toomre & Toomre (1972)
				kin2	Toomre (1978)
				qual	Hernquist (1990b),
				kin2	Salo & Laurikainen (2000)
				gen	Wahde & Donner (2001)
				gen	Theis & Spinnaker (2003)
				kin2	Durrell et al. (2003)
NGC 5216/18	104	033	E+S	qual	Cullen et al. (2007)
NGC 5394/95	084	048	S+S	qual	Kaufman et al. (1999)
AM 2004-662			E+d	kin1	Díaz et al. (2000)
NGC 6872 / IC 4970			S+S0	qual	Mihos et al. (1993)
				qual	Horellou & Koribalski (2007)
NGC 7252	226		S+S	qual	Borne & Richstone (1991)
				qual	Mihos et al. (1993)
				kin2	Hibbard & Mihos (1995)
				qual	Mihos et al. (1998)
NGC 7714/15	284	051	ring	qual	Smith & Wallin (1992)
				kin2	Struck & Smith (2003)
NGC 7752/53	086	005	S+d	kin2	Salo & Laurikainen (1993)

Notes.

^a This table attempts to survey and characterize dynamical models of interacting galaxies which make significant use of kinematic constraints. Different authors often use very different criteria when imposing kinematic constraints, and published descriptions are sometimes ambiguous. No warranty of completeness is expressed or implied.

^b In this column, a slash separates components of a given system, while a comma separates alternate names. NGC numbers are used when available; if all components have NGC numbers, the full number is given for the first galaxy, and only the last two digits for the rest.

^c Briefly, “kin2” matches are constrained by two-dimensional kinematic data, “kin1” matches are constrained by one-dimensional kinematic data, “gen” matches used genetic algorithms, “qual” matches reproduce qualitative kinematic features, and “morph” matches reproduce morphology (listed *only* as precursors). See text for details.

^d Type of companion is ambiguous.

^e Identity of companion is ambiguous.

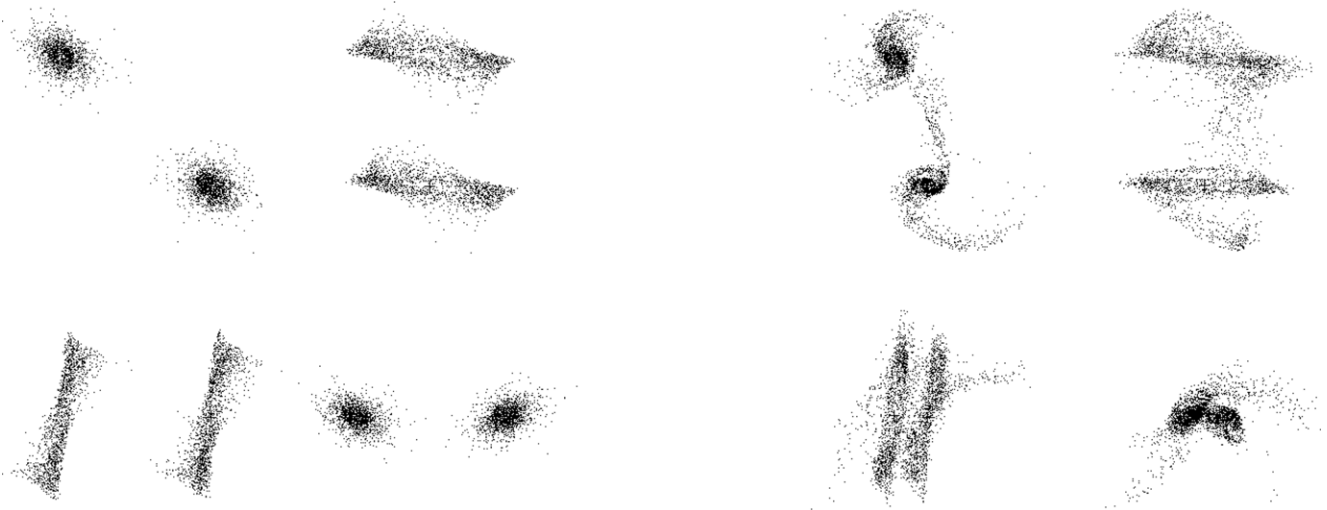


Figure 14. Identikit simulation showing how a tidal encounter breaks degeneracy in disk orientations. The system is viewed along the orbital axis. The disks have inclinations $i_1 = 45^\circ$ and $i_2 = 135^\circ$ and arguments $\omega_1 = \omega_2 = 30^\circ$. Left: one time unit before pericenter; note that both disks present the same appearance on the (X, Y) , (V, Y) , and (X, V) planes (top left, top right, and bottom left, respectively), although the (X, Z) projection (bottom right) shows that they do not have the same orientation in space. Right: one time unit after pericenter; the difference between the two disks is now evident in all four projections.

optimal ensemble, with the fittest individual representing the best approximation to the desired solution.

Genetic algorithms for modeling interacting galaxies have been tested on artificial data (Wahde 1998; Theis & Kohle 2001; Gomez et al. 2002) and applied to real data for NGC 4449 (Theis & Kohle 2001) and NGC 5194/95 (Wahde & Donner 2001; Theis & Spinnaker 2003). Typical values of $N_{\text{pop}} \simeq 10^2$ and $N_{\text{gen}} \simeq 10^2$ imply that $\sim 10^4$ individuals must be evaluated to obtain a good match; with test-particle methods, this can be done in a few hours of CPU time. The Identikit methodology (Section 2) could be combined with a genetic algorithm, improving the treatment of orbital decay and substantially reducing the CPU time required to find a match.

However, the output of a genetic algorithm will be no better than the evaluation function $\mathcal{F}(\mathcal{P}, \mathcal{D})$ used to determine fitness. The simplest approach is to coarsely grid \mathcal{P} on the (X, Y) plane, and compare the result with an equally coarse gridding of \mathcal{D} . More recent implementations incorporate velocity information as well, and there is no reason why gridding can not be extended to three-dimensional (X, Y, V) data. But the first two limitations of the Identikit method noted above also apply to existing evaluation functions. Features due to self-gravity in real systems can be discounted by an expert when attempting to fit a test-particle model, but may mislead an objective evaluation function, lowering the fitness of accurate solutions. And while H I is a good tracer of kinematics, its distribution in tidal features is often quite irregular; for example, a tail may appear as a series of clumps rather than a connected structure. An expert can recognize such tails as connected structures, but an automatic procedure may reject solutions which populate them with a smooth distribution of particles. To address these problems, recent genetic algorithm implementations include routines for masking or weighting the observational data; it remains to be seen if these techniques make genetic algorithms competitive with human experts.

4.3. Are Models Unique?

Can a dynamical model reproducing the morphology and kinematics of an interacting pair of galaxies be considered unique? Claims to this effect occasionally appear (e.g., Borne 1988a, 1988b; Theis & Kohle 2001); skeptics, paraphrasing

John von Neumann⁸, may be tempted to reply “with that many parameters I could fit an elephant.” The 16 parameters introduced in Section 1 are all physically motivated and necessary to describe a collision of two disk galaxies in three dimensions; if a large number of parameters per se was really a flaw, models of spectral line formation in stellar atmospheres, requiring up to ~ 90 abundance parameters, would be on shaky ground indeed. Yet claims of uniqueness seem overconfident. A particular match may be unique within the universe of possibilities defined by a given model, implying that all the parameters appearing in the model can be determined within reasonable accuracy, and that no set of parameters outside this tolerance range yield as good a match. However, this is *not* the same thing as uniquely determining the dynamical state of a pair of colliding galaxies, which is specified by the distribution function $f(\mathbf{r}, \mathbf{v})$.

The problem of dynamically modeling isolated early-type galaxies, which has generated an extensive literature, illustrates some of the difficulties involved in determining $f(\mathbf{r}, \mathbf{v})$. Recent studies (e.g., van de Ven et al. 2008; van den Bosch et al. 2008) use Schwarzschild’s (1979) method to fit models with equilibrium distribution functions depending on three integrals of motion to stellar velocity data obtained from integral field spectroscopy. Such models are quite successful at describing the orbital structure of galaxies and diagnosing the presence of black holes and dark halos. But not many of these models are truly unique; the orientations and intrinsic shapes of axisymmetric models appear uncertain (Krajnović et al. 2005; van den Bosch et al. 2008), while triaxial models pose additional difficulties (van de Ven et al. 2008). Determining $f(\mathbf{r}, \mathbf{v})$ for one galaxy is hard; doing so for a pair of galaxies seems harder still.

In the context of the model described here, it may not even be obvious that we can hope to constrain even the most basic parameters. The orientation of a single disk, unless it happens to be exactly edge-on, cannot be determined from a data cube $F(X, Y, V)$; for example, a disk tilted by 45° to the line of sight produces *exactly* the same data cube as one tilted by 135° (this ambiguity can be resolved by using dust lanes to

⁸ See Dyson (2004, p. 297) for one version: “with four parameters I can fit an elephant and with five I can make him wiggle his trunk.” John von Neumann could presumably fit a whole herd of elephants with the parameters used to describe a single galactic encounter.

determine which side of the disk is closer, although doing so goes beyond a strictly kinematic approach to galaxy modeling; see e.g., the discussion in Struck et al. 2005). By extension, a pair of disks yield a four-fold degenerate solution, since each disk has two possible orientations. However, tidal interactions between disks break this degeneracy; as Figure 14 shows, two disks which initially display identical $F(X, Y, V)$ distributions can be differentiated *after* an encounter. In this example, as in most of our Identikit solutions, the disk orientations (i_1, ω_1) and (i_2, ω_2) are strongly constrained; a little “wiggle room” exists around the actual values, but no radically different choice can reproduce the “observed” morphology and kinematics.

Taken together, the results in Section 3.3 shows that almost all of our 18 “good” and 12 “fair” fits accurately constrain the disk orientations, viewing direction, time since pericenter, pericentric separation, and scale factors. We did not examine errors in center-of-mass position and velocity, but the offsets in our fits were always very small, so presumably these parameters are also well constrained. While some solutions are better than others, all 30 of these fits appear to be unique; the estimated parameters are always in the neighborhood of the actual values, and often very close indeed.

The six “poor” fits tell a different story. Object 16 (see Figure 2), a wide retrograde encounter “observed” long after pericenter, has such attenuated tidal features that fitting this system is much like fitting a pair of disks *before* their first encounter; our fit is clearly degenerate. As Section 3.5 describes, object 6 also produced nonunique fits. Other poor solutions may also be degenerate, in view of the large misalignments in viewing direction and disk orientation that they display (see Figures 6 and 7).

The fact that we were able to produce well constrained and reasonably accurate solutions for 30 out of 36 systems depends critically on the quality of the “observational” data we used. Data with lower resolution and added noise would yield a less favorable outcome; in particular, incomplete velocity information can seriously compromise a solution. Models of NGC 7252 illustrate this point; early attempts using very limited velocity data concluded that this object resulted from a merger of two *retrograde* disks (Borne & Richstone 1991), but once high-quality H I data became available a very convincing solution involving a collision of two *direct* disks was soon found (Hibbard & Mihos 1995). Fortunately, instruments such as the Expanded Very Large Array now coming online should make it far easier to obtain the detailed velocity information needed to accurately constrain dynamical models of interacting galaxies.

However, even a surfeit of data will not guarantee an unambiguous model in every case. One example may be the “Whirlpool” galaxy, NGC 5194/95; after three and a half decades of modeling based on ever-better H I data there is still no consensus regarding the number of passages required to account for NGC 5194’s optical morphology *and* extended H I tail (e.g., Durrell et al. 2003, and references therein). Models in which NGC 5195 makes only one passage can account for many of the observations but have trouble matching the tail velocities, while models in which this galaxy makes *two* passages match the velocities better but yield double tails (see Salo & Laurikainen 2000, Figure 4). One possible solution to this puzzle is to assume that NGC 5194’s H I disk was warped even *before* its first and only encounter with NGC 5195; this could tilt the tail with respect to the inner disk in such a way as to match the observed velocities. Of course, pre-existing warps vastly complicate questions of uniqueness. In the specific case

of NGC 5194/95, stronger evidence in favor of a single passage seems necessary to justify introducing such a warp; better data on *stellar* velocities may help (Durrell et al. 2003).

Our limited knowledge of dark matter is a more fundamental barrier to the creation of truly unique models for interacting galaxies. Models of isolated galaxies in equilibrium can represent the dark matter as a potential imposed by hand. In contrast, models of interacting systems should really treat dark matter as a full participant in the dynamical equations.⁹ Given how little we know about dark matter, a good deal of guess-work will be part of any such model, and this is unlikely to change unless we can somehow measure the detailed distribution *and* kinematics of dark matter in individual galaxies. Nonetheless, models of interacting galaxies have already set limits on the radial structure of dark halos (Dubinski et al. 1996; Mihos et al. 1998; Barnes 1999; Springel & White 1999), and further studies may yield additional insights into the nature, distribution, and dynamics of dark matter.

While it may never be possible to determine a unique distribution function $f(\mathbf{r}, \mathbf{v})$ for a specific pair of interacting galaxies, there are still compelling reasons to construct detailed models. A good model of a galactic collision can serve as a unifying hypothesis, providing a context to integrate and interpret a variety of observations; for example, a time-line of past encounters may help to understand interaction-induced star formation. Conversely, a bad model which contradicts other lines of evidence can be rejected. Viewed as a means to an end, dynamical modeling stands to teach us a good deal about galactic encounters and galaxies in general.

4.4. Extensions

While the current Identikit system is essentially an interactive modeling tool, the basic approach offers other possibilities. For example, once the orbital parameters p, e , and μ , time t , viewing angles ($\theta_X, \theta_Y, \theta_Z$), and scale factors \mathcal{L} and \mathcal{V} have been fixed, it is possible to invert the mapping from initial disk orientation (i, ω) to the data cube $F(X, Y, Z)$, and ask which (i, ω) values allow a disk to populate a given point in the (X, Y, V) space. As a rule, each (X, Y, V) point corresponds to some range of (i, ω) values, but *different* points along one tidal structure should all be populated by the *same* disk, so this range can be constrained. This approach could effectively automate the process of finding disk orientations once other parameters have been selected; it could particularly useful in establishing confidence limits for key parameters once an initial match has been determined.

The Identikit technique has some interesting similarities to the Schwarzschild (1979) method for building triaxial equilibrium systems. In a nutshell, Schwarzschild started with a stationary mass model, populated it with all possible orbits, and figured out how to add up the time-averaged density distributions of these orbits so as to recover the original mass model. We start with a time-dependent mass model generated by an encounter of two spherical systems; each sphere is initially populated with all possible circular orbits. But instead of finding a weighted sum of these orbits which reproduces the mass distribution, we try to select one coplanar family of orbits from each sphere to match the observed kinematics and morphology of interacting galaxies. Perhaps some variant of the algorithms used in Schwarzschild’s method to determine orbital weights could be applied to the problem of modeling interacting galaxies.

⁹ To be sure, not every study in Table 2 did this, but the speed of modern computers leaves little excuse for not treating the dark matter self-consistently in future work.

We hope to implement some of these extensions in Identikit 2.

J.E.B. thanks François Schweizer, Breannán Nualláin, Shin Mineshige, and Piet Hut for valuable conversations and comments, and the Observatories of the Carnegie Institute of Washington, the California Institute of Technology, Kyoto University, and the Japan Society for the Promotion of Science for support and hospitality. We thank Curtis Struck for an open and constructive referee report. The National Radio Astronomy Observatory is a facility of The National Science Foundation operated under cooperative agreement by Associated Universities, Inc.

APPENDIX A

IDENTIKIT MODEL CONSTRUCTION

To set up initial conditions for Identikit models we need to construct spherical equilibrium N -body models with the mass profiles $m(r)$ given by Equation (2). We use the Eddington (1916) formula (e.g., Binney & Tremaine 1987, p. 236) to compute the distribution function $f(E)$. Kazantzidis et al. (2004) used this approach to construct equilibrium halos with density profiles described by a three-parameter family of models (e.g., Zhao 1996). We go one step further by correcting for the finite resolution (i.e., “softening”) of the N -body force calculation.

We account for the effect of Plummer softening (Aarseth 1963; Hernquist & Barnes 1990) in the N -body simulations by introducing a quasiempirical transformation of the total mass profile (J. E. Barnes 2010, in preparation):

$$\bar{m}(r) = [1 + (2/3)^{(\kappa/\alpha)} (\tilde{\epsilon}/r)^\kappa]^{(\alpha/\kappa)} m(r), \quad (\text{A1})$$

where α is the logarithmic derivative of the density profile as $r \rightarrow 0$, the parameter $\tilde{\epsilon}$ is comparable to the softening length ϵ , and the parameter κ adjusts the shape of the transition near $r \sim \tilde{\epsilon}$. This smoothed mass profile is then used to compute the potential

$$\frac{d\Phi}{dr} = G \frac{\bar{m}(r)}{r^2}, \quad (\text{A2})$$

where $\Phi \rightarrow 0$ as $r \rightarrow \infty$. After expressing the original density profile $\rho(r) = (4\pi r^2)^{-1} dm/dr$ as a function of this potential Φ , we compute the distribution function

$$f(E) = \frac{1}{\sqrt{8\pi^2}} \frac{d}{dE} \int_E^0 d\Phi (\Phi - E)^{-1/2} \frac{d\rho}{d\Phi}. \quad (\text{A3})$$

Once $f(E)$ has been calculated, generating an N -body realization with N_{sphr} massive particles is straightforward. For each particle i , let $\hat{\mathbf{r}}_i$ and $\hat{\mathbf{v}}_i$ be two vectors drawn from a uniform distribution on the unit sphere \mathbb{S}^2 . Then the position of particle i is $\mathbf{r}_i = r_i \hat{\mathbf{r}}_i$, where r_i is chosen by drawing a random number x from a uniform distribution in the range $[0, m(\infty)]$ and solving $m(r_i) = x$, and the velocity is $\mathbf{v}_i = v_i \hat{\mathbf{v}}_i$, where v_i is chosen from the speed distribution $v^2 f(\frac{1}{2}v^2 + \Phi(r_i))$ using rejection sampling (von Neumann 1951). The particle masses are $m_i = m(\infty)/N_{\text{sphr}}$.

The N_{test} test particles are initially placed in a single disk. If the test-particle distribution follows $m_d(r)$, the initial radius q_i of particle i may be selected by drawing a random number x from a uniform distribution in the range $[0, m_d(\infty)]$ and solving $m_d(q_i) = x$. However, we prefer to bias the distribution by a

factor of r^2 to improve disk sampling at large r (see Section 2). Let

$$\eta(r) = \int_0^r d\chi \chi^2 m'_d(\chi), \quad (\text{A4})$$

where $m'_d(r) = dm_d/dr$; then q_i is selected by drawing x from $[0, \eta(\infty)]$ and solving $\eta(q_i) = x$. The orbital velocity v_i of particle i is calculated using the smoothed profile:

$$v_i = \sqrt{G \bar{m}(q_i)/q_i}. \quad (\text{A5})$$

Note that test particles are placed on *exactly* circular orbits, creating a perfectly “cold” disk. Finally, the position \mathbf{r}_i and velocity \mathbf{v}_i of particle i are rotated to align $\mathbf{r}_i \times \mathbf{v}_i$ with a normalized angular momentum $\hat{\mathbf{s}}_i$ drawn from a uniform distribution on \mathbb{S}^2 .

APPENDIX B

RANDOM MERGER MODELS

Our galaxy construction procedure has some elements in common with McMillian & Dehnen (2007). Like them, we compute isotropic distribution functions $f_b(E)$ and $f_h(E)$ for the bulge and halo, respectively, by approximating the disk’s gravitational field with its spherically averaged equivalent. Unlike them, we use the resulting bulge and halo “as is,” without first adiabatically imposing a flattened disk potential; the response of the bulge and halo to such an adiabatic transformation is so subtle that a good approximation to equilibrium is possible without it. This makes our procedure quite fast. What follows is a brief technical description of our procedure; a full discussion and numerical tests will be presented elsewhere (J. E. Barnes 2010, in preparation).

The bulge follows a Hernquist (1990a) model out to a radius b_b , and tapers at larger radii to avoid placing a small number of particles at extremely large distances:

$$\rho_b(r) = \begin{cases} \frac{a_b m_b}{2\pi} \frac{1}{r(a_b + r)^3}, & r \leq b_b \\ \rho_b^* \left(\frac{b_b}{r}\right)^2 e^{-2r/b_b}, & r > b_b, \end{cases} \quad (\text{B1})$$

where m_b is the bulge mass, and ρ_b^* is fixed by requiring that $\rho_b(r)$ be continuous at $r = b_b$. For $b_b \gg a_b$, the slope $d\rho_b/dr$ is also continuous at $r = b_b$.

The halo follows a Navarro et al. (1996) model out to a radius b_h , and tapers at larger radii as proposed by Springel & White (1999):

$$\rho_h(r) = \begin{cases} \frac{m_h(a_h)}{4\pi \left(\ln(2) - \frac{1}{2}\right)} \frac{1}{r(r + a_h)^2}, & r \leq b_h \\ \rho_h^* \left(\frac{b_h}{r}\right)^\beta e^{-r/a_h}, & r > b_h, \end{cases} \quad (\text{B2})$$

where $m_h(a_h)$ is the halo mass within radius a_h , and ρ_h^* and β are fixed by requiring that both $\rho_h(r)$ and $d\rho_h/dr$ be continuous at $r = b_h$. The halo is tapered more abruptly than the bulge to tame the logarithmic divergence of the standard Navarro et al. mass profile as $r \rightarrow \infty$.

The disk has an exponential radial profile (de Vaucouleurs 1959a, 1959b; Freeman 1970) and a sech^2 vertical profile (van der Kruit & Searle 1981):

$$\rho_d(q, \phi, z) = \frac{m_d}{4\pi a_d^2 z_d} e^{-q/a_d} \text{sech}^2\left(\frac{z}{z_d}\right), \quad (\text{B3})$$

where $(q = \sqrt{x^2 + y^2}, \phi, z)$ are cylindrical coordinates and m_d is the total mass of the disk.

For the bulge and halo, cumulative mass profiles are obtained by integrating Equations (B1) and (B2):

$$\begin{aligned} m_b(r) &= \int_0^r d\chi \, 4\pi \chi^2 \rho_b(\chi), \quad \text{and} \\ m_h(r) &= \int_0^r d\chi \, 4\pi \chi^2 \rho_h(\chi). \end{aligned} \quad (\text{B4})$$

We use the cumulative mass profile for an infinitely thin disk,

$$m_d(r) = m_d (1 - e^{-r/a_d})(1 + r/a_d), \quad (\text{B5})$$

which is adequate for our purposes since $m_b(r) \gg m_d(r)$ at small r . These functions are summed to get the total mass profile $m(r)$, the smoothed profile $\bar{m}(r)$ is computed using Equation (A1), and the potential $\Phi(r)$ is computed using Equation (A2). We then express ρ_b and ρ_h as functions of Φ , insert these functions in Equation (A3) to obtain $f_b(E)$ and $f_h(E)$, and construct N -body realizations of the bulge and halo following the procedure described in Appendix A.

The disk is realized by sampling an approximate distribution function

$$\begin{aligned} f_d(q, \phi, z, v_q, v_\phi, v_z) &\propto \rho_d(q, \phi, z) \mathcal{H} \left[\frac{v_q}{\sigma_q(q)} \right] \\ &\times \mathcal{H} \left[\frac{v_\phi - \bar{v}(q)}{\sigma_\phi(q)} \right] \mathcal{G} \left[\frac{v_z}{\sigma_z(q)} \right], \end{aligned} \quad (\text{B6})$$

where v_q , v_ϕ , and v_z are velocities in the radial, azimuthal, and vertical directions, respectively. The function $\bar{v}(q)$ is the mean rotation velocity, while $\sigma_q(q)$, $\sigma_\phi(q)$, and $\sigma_z(q)$ are dispersions in the radial, azimuthal, and vertical directions, respectively. The function $\mathcal{G}(x)$ is a Gaussian, while $\mathcal{H}(x)$ resembles $\mathcal{G}(x)$ but cuts off faster for large $|x|$:

$$\mathcal{G}(x) \propto e^{-\frac{1}{2}x^2}, \quad \mathcal{H}(x) \propto e^{-\frac{1}{2}(x/c)^2 - \frac{1}{4}(x/c)^4}, \quad (\text{B7})$$

where c is fixed by requiring $\int dx \, x^2 \mathcal{H}(x) = \int dx \, \mathcal{H}(x)$. This function is used instead of a Gaussian to avoid overpopulating the high-velocity tail of the distribution.

The local circular velocity $v_c(q)$ is given by

$$v_c^2(q) = G \frac{\bar{m}_s(q)}{q} + q \frac{d\Phi_d}{dq}, \quad (\text{B8})$$

where $\bar{m}_s(q)$ is the smoothed spheroid (bulge + halo) mass profile and Φ_d is the potential due to the disk. To compute $\bar{m}_s(r)$ we insert the spheroid profile $m_s(r) = m_b(r) + m_h(r)$ in Equation (A1). Our expression for Φ_d explicitly takes “softening” into account:

$$\frac{d\Phi_d}{dq} = -\frac{Gm_d}{a_d^3} \int_0^\infty dk \frac{k e^{-k\epsilon_d} J_1(kq)}{(a_d^{-2} + k^2)^{3/2}}, \quad (\text{B9})$$

where $J_1(x)$ is the cylindrical Bessel function of order 1, and setting $\epsilon_d = \sqrt{\epsilon^2 + z_d^2}$ allows—in an approximate way—for the finite thickness of the disk.

The vertical dispersion is given by the solution for an isothermal sheet (e.g., Binney & Tremaine 1987, p. 282):

$$\sigma_z(q) = \sqrt{\pi G z_d \Sigma(q)}, \quad (\text{B10})$$

where $\Sigma(q) = \int dz \, \rho_d(q, z)$ is the surface density of the disk at cylindrical radius q . The radial dispersion is then determined by fixing the ratio σ_q/σ_z :

$$\sigma_q(q) = \mu(q) \sigma_z(q) = \left(1 + \frac{q}{q + q_\sigma}\right) \sigma_z(q), \quad (\text{B11})$$

where q_σ is a scale parameter comparable to a_d . The function $\mu(q)$ is chosen to make $\sigma_q/\sigma_z \simeq 2$ in the body of the disk—roughly matching the solar neighborhood value (e.g., Dehnen & Binney 1998)—while letting $\sigma_q/\sigma_z \rightarrow 1$ for $q \rightarrow 0$. The azimuthal dispersion is related to the radial dispersion (Binney & Tremaine 1987, p. 203):

$$\sigma_\phi(q) = \frac{\kappa(q)}{2\Omega(q)} \sigma_q(q), \quad (\text{B12})$$

where $\Omega(q) = v_c(q)/q$ is the circular orbital frequency and $\kappa(q) = \sqrt{4\Omega^2 + q d\Omega^2/dq}$ is the epicyclic frequency.

Finally, the mean rotation velocity $\bar{v}(q)$ is determined using the axisymmetric Jeans equation (e.g., Binney & Tremaine 1987, p. 198):

$$\bar{v}^2(q) = v_c^2(q) + \sigma_q^2(q) \left(1 - \frac{2q}{a_d}\right) - \sigma_\phi^2(q) + \sigma_z^2(q) q \frac{d\mu^2}{dq}. \quad (\text{B13})$$

The parameter values needed to completely define the galaxy model are

$$\begin{aligned} m_b &= 0.0625, & a_b &= 0.02, & b_b &= 4.0, \\ m_d &= 0.1875, & a_d &= 1/12, & z_d &= 0.0075, \\ m_h(a_h) &= 0.16, & a_h &= 0.25, & b_h &= 0.98015, \\ \epsilon &= 0.0075, & \tilde{\epsilon} &= 0.0115, & \tilde{\epsilon}_s &= 0.0115, \\ q_\sigma &= 0.075, & \kappa &= 1.975, & \kappa_s &= 2.025. \end{aligned} \quad (\text{B14})$$

A few remarks about these parameters are in order. First, tapering the bulge as in Equation (B1) with $b_b = 200a_b$ reduces the total bulge mass by $\sim 0.5\%$; to correct this, the value of m_b actually used in Equation (B1) is adjusted upward accordingly. Second, the primary halo-mass parameter is $m_h(a_h)$; the halo taper radius b_h is adjusted to make the total halo mass $m_h(\infty) = m_h = 1.0$. Third, the softening parameter actually used in the N -body calculations is ϵ ; the values of $\tilde{\epsilon}$ and κ listed here are chosen by computing $\Phi(r)$ using Equation (A2) and comparing the result to an N -body calculation. Fourth, the parameters $\tilde{\epsilon}_s$ and κ_s used to compute the smoothed spheroid mass profile $\bar{m}_s(r)$ are likewise chosen by comparison with an N -body calculation.

Figure 15 presents circular velocity profiles for the galaxy model adopted here. The left-hand panel shows profiles for the individual components, computed taking softening into account as described above. Also shown is the total circular velocity $v_c(q)$ given by Equation (B8). The right-hand panel again shows $v_c(q)$ and compares it with the mean rotation velocity $\bar{v}(q)$ given by Equation (B13) and the circular velocity for the equivalent spherical mass model given by Equation (A5).

To check this model, we constructed a realization with $N_b = 16384$ bulge particles, $N_d = 49152$ disk particles, and $N_h = 65536$ halo particles. This system was then evolved in isolation for 10 time units, using a hierarchical N -body code¹⁰ with an

¹⁰ See <http://www.ifa.hawaii.edu/faculty/barnes/treecode/treeguide.html> for a discussion of this code, which generalizes earlier modifications (Barnes 1990) of the original tree code (Barnes & Hut 1986).

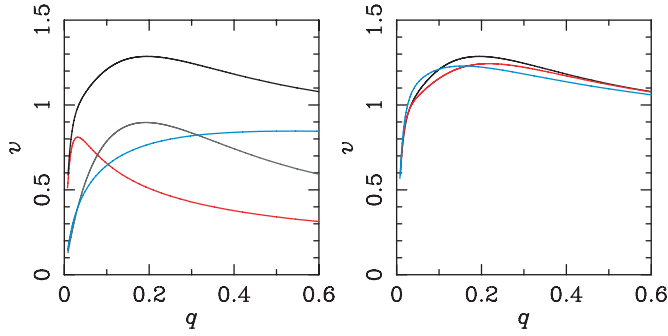


Figure 15. Circular velocity profiles for the disk galaxy model. Left: circular velocities for the bulge (red), disk (gray), and halo (blue). The total circular velocity is also shown (black). Right: total circular velocity (black), mean rotation velocity (red), and circular velocity for the spherical mass model (blue). (A color version of this figure is available in the online journal.)

accuracy parameter $\theta = 1$, quadrupole-moment corrections (Hernquist 1987), a Plummer softening length $\epsilon = 0.0075$, and a leap-frog integrator with a time-step $\Delta t = 1/256$. During the first 0.25 time units the ratio of kinetic to potential energy, T/U , fell from an initial value of 0.4980–0.4945; it then fluctuated around this value with an amplitude of ~ 0.003 . This initial drop indicates that the model was not started in perfect equilibrium, but the implied rearrangement of mass is only a little larger than the $1/\sqrt{N}$ ($\simeq 0.0028$) fluctuations occurring in an N -body system with this N . Apart from transient spiral structure, this model showed no significant features until the disk begins to develop a bar at time $t \simeq 4$. It is hard to completely suppress a weak bar instability in galaxy models with relatively massive

disks such as the one used here; however, this instability has little effect on the merger simulations since the galaxies interact with each other long before they would develop bars in isolation.

The 36 random merger simulations were run with the same number of particles per galaxy and N -body integration parameters used in the test just described. Energy was conserved to $\sim 0.05\%$ even in the most violent encounters. Particle positions and velocities were output every $\Delta t_{\text{out}} = 1/32$ time units, providing a large database which could be used to construct random samples such as the one in Figure 2.

APPENDIX C

VELOCITY SCALE BIAS

As noted at the end of Section 3.3, Identikit estimates of the velocity scale \mathcal{V} are typically $\sim 10\%$ too high. The value of \mathcal{V} is usually determined toward the end of the matching process; after values have been selected for most other parameters, we adjust \mathcal{V} to obtain a good overall match between the particles and the gray-scale images in the (X, V) and (V, Y) planes. There are a number of factors which may influence the choice for \mathcal{V} , including the velocity difference between the galaxies and the characteristic velocities of tidal features. However, a key feature is the velocity widths of the galaxies; we generally try to adjust \mathcal{V} so that the particles span the full range of velocities present in each galaxy.

While matching the velocity widths of the individual galaxies *seems* reasonable, it appears to be the source of the bias in \mathcal{V} . Velocities in the test-particle Identikit disks are not identical to those in the self-gravitating disks used in the random mergers; the former are perfectly “cold,” while the latter have nonzero

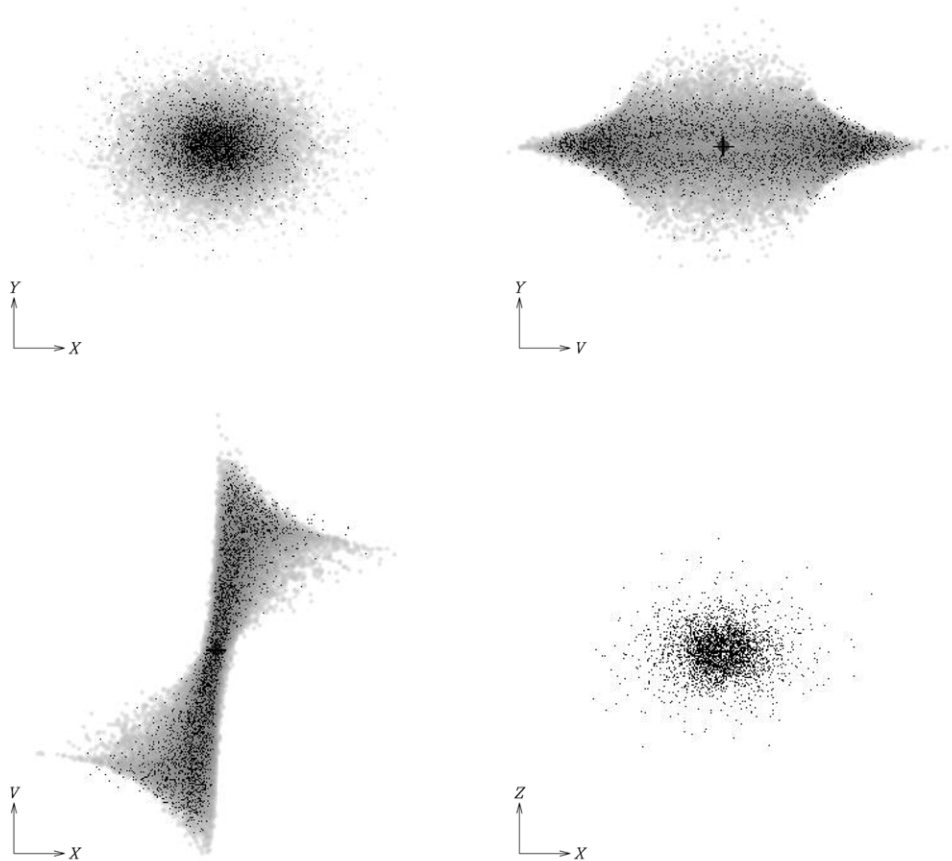


Figure 16. Identikit match to a single disk galaxy. The velocity scale factor \mathcal{V}_{fit} was adjusted by eye to match the width of the velocity distribution.

velocity dispersions. In addition, as the right-hand panel in Figure 15 shows, the circular velocity profile of the Identikit model rises more rapidly, peaks at a smaller radius, and then falls slightly below either the circular ($v_c(q)$) or mean ($\bar{v}(q)$) profiles in the self-gravitating model.

Figure 16 shows an Identikit fit to a self-consistent disk galaxy model. This disk is tilted by 45° to the line of sight; in fitting this model, the orientation and length scale factor were first set to their actual values. We then adjusted \mathcal{V}_{fit} by eye, stretching the particle distribution to match the apparent velocity width of the gray-scale images in the (X, V) and (V, Y) projections. The value of \mathcal{V}_{fit} selected in this manner is 10.9% too high, much as in the Identikit matches to interacting galaxies. In hindsight, we note that the (X, V) projection shows a handful of points falling outside the rotation curve for large $|X|$; a fit giving priority to these points would have recovered a more accurate value for \mathcal{V} .

Compared to its Identikit analog, the larger velocity width of the self-consistent disk is a direct consequence of the random velocities imparted to individual disk particles. To test this, we constructed self-consistent disks with different dispersions and velocity scales, and selected best-fit values of \mathcal{V}_{fit} as in Figure 16. The ratio $\mathcal{V}_{\text{fit}}/\mathcal{V}_{\text{true}}$ has a one-to-one relationship with the disk's velocity dispersion; the larger the dispersion, the greater the overestimate of \mathcal{V} . It is likely that by constructing Identikit models with random velocities comparable to those present in the self-gravitating disks we could largely remove this bias. However, “cold” disks may actually be more appropriate when fitting kinematics observed in cold gas tracers (e.g., H I or CO), since these have smaller velocity dispersions than most stellar components.

REFERENCES

- Aarseth, S. J. 1963, *MNRAS*, **126**, 223
- Antunes, A., & Wallin, J. 2007, *ApJ*, **670**, 261
- Appleton, P. N., & Struck-Marcell, C. 1996, *Fund. Cos. Phys.*, **16**, 111
- Barnes, J. E. 1988, *ApJ*, **331**, 699
- Barnes, J. E. 1990, *J. Comput. Phys.*, **87**, 161
- Barnes, J. E. 1992, *ApJ*, **393**, 484
- Barnes, J. E. 1998, in *Galaxies: Interactions and Induced Star Formation, Dynamics of Galaxy Interactions*, ed. D. Friedli, L. Martinet, & D. Pfenniger (Berlin: Springer), 275
- Barnes, J. E. 1999, in *Galaxy Interactions at Low and High Redshift, Dynamics of Mergers and Remnants*, ed. J. E. Barnes & D. B. Sanders (Dordrecht: Kluwer), 137
- Barnes, J. E. 2004, *MNRAS*, **350**, 798
- Barnes, J., & Hut, P. 1986, *Nature*, **324**, 446
- Binney, J., & Tremaine, S. 1987, *Galactic Dynamics* (Princeton, NJ: Princeton Univ. Press)
- Borne, K. D. 1984, *ApJ*, **287**, 503
- Borne, K. D. 1988a, *ApJ*, **330**, 38
- Borne, K. D. 1988b, *ApJ*, **330**, 61
- Borne, K. D., & Richstone, D. O. 1991, *ApJ*, **369**, 111
- Brouillet, N., Baudry, A., Combes, F., Kaufman, M., & Bash, F. 1991, *A&A*, **242**, 35
- Casertano, S., & van Gorkom, J. H. 1991, *AJ*, **101**, 1231
- Catinella, B., Giovanelli, R., & Haynes, M. P. 2006, *ApJ*, **640**, 751
- Clemens, M. S., Baxter, K. M., Alexander, P., & Green, D. A. 1999, *MNRAS*, **308**, 364
- Combes, F., Foy, F. C., Weliachew, L., & Gottesman, S. T. 1980, *A&A*, **84**, 85
- Combes, F., Dupraz, C., Casoli, F., & Pagani, L. 1988, *A&A*, **203**, L9
- Cullen, H., Alexander, P., Green, D. A., & Sheth, K. 2007, *MNRAS*, **376**, 98
- de Vaucouleurs, G. 1959a, *Handbuch der Physik*, **53**, 311
- de Vaucouleurs, G. 1959b, *ApJ*, **130**, 728
- Dehnen, W., & Binney, J. J. 1998, *MNRAS*, **298**, 387
- Díaz, R., Rodrigues, I., Dottori, H., & Carranza, G. 2000, *AJ*, **119**, 111
- Dubinski, J., Mihos, J. C., & Hernquist, L. 1996, *ApJ*, **462**, 576
- Duc, P.-A., & Bouchaud, F. 2008, *ApJ*, **673**, 787
- Duc, P.-A., Brinks, E., Springel, V., Pichardo, B., Weilbacher, P., & Mirabel, I. F. 2000, *AJ*, **120**, 1238
- Durrell, P. R., Mihos, J. C., Feldmeier, J. J., Jacoby, G. H., & Ciardullo, R. 2003, *ApJ*, **582**, 170
- Dyson, F. 2004, *Nature*, **427**, 297
- Eddington, A. S. 1916, *MNRAS*, **76**, 572
- Elmegreen, B. G., Sundin, M., Kaufman, M., Brinks, E., & Elmegreen, D. M. 1995, *ApJ*, **453**, 139
- Farouki, R. T., & Shapiro, S. L. 1982, *ApJ*, **259**, 103
- Freeman, K. C. 1970, *ApJ*, **160**, 811
- Gilbert, S. J., & Sellwood, J. A. 1994, in *Numerical Simulations in Astrophysics: Modelling the Dynamics of the Universe*, ed. J. Franco, S. Lizano, L. Aguilar, & E. Daltabuit (Cambridge: Cambridge Univ. Press), 131
- Gomez, J. C., Fuentes, O., & Puerari, I. 2002, in *Astronomical Data Analysis Software and Systems XI, Determination of Orbital Parameters of Interacting Galaxies Using Evolution Strategies*, ed. D. A. Bohlender, D. Durand, & T. H. Handley (San Francisco: CA: ASP), 409
- Günthardt, G. I., Agüero, E. L., Rodrigues, I., & Díaz, R. J. 2006, *A&A*, **453**, 801
- Hearn, N. C., & Lamb, S. A. 2001, *ApJ*, **551**, 651
- Hernquist, L. 1987, *ApJS*, **64**, 715
- Hernquist, L. E. 1990a, *ApJ*, **356**, 359
- Hernquist, L. 1990b, in *Dynamics and Interactions of Galaxies, Dynamical status of M51*, ed. R. Wielen (Springer: Heidelberg), 108
- Hernquist, L., & Barnes, J. E. 1990, *ApJ*, **349**, 562
- Hernquist, L., & Quinn, P. J. 1987, *ApJ*, **312**, 1
- Hibbard, J. E. 2003, *BAAS*, **35**, 1413
- Hibbard, J. E., & Mihos, J. C. 1995, *AJ*, **110**, 140
- Hibbard, J. E., Guhathakurta, P., van Gorkom, J. H., & Schweizer, F. 1994, *AJ*, **107**, 67
- Hibbard, J. E., van Gorkom, J. H., Rupen, M. P., & Schiminovich, D. S. 2001, in *ASP Conf. Ser. 240, An H I Rouges Gallery, Gas & Galaxy Evolution*, ed. J. E. Hibbard, M. P. Rupen, & J. H. van Gorkom (San Francisco, CA: ASP), 659
- Holland, J. H. 1975, in *Adaptation in Natural and Artificial Systems* (1st ed.; Ann Arbor, MI: Univ. Michigan Press)
- Holland, J. H. 1992, in *Adaptation in Natural and Artificial Systems* (2nd ed.; Cambridge, MA: MIT Press)
- Horellou, C., & Koribalski, B. 2007, *A&A*, **464**, 155
- Howard, S., Keel, W. C., Byrd, G., & Burke, J. 1993, *ApJ*, **417**, 502
- Hui, X., Ford, H. C., Freeman, K. C., & Dopita, M. A. 1995, *ApJ*, **449**, 592
- Kaufman, M., Brinks, E., Elmegreen, B. G., Elmegreen, D. M., Klarić, M., Struck, C., Thomasson, M., & Vogel, S. 1999, *AJ*, **118**, 1577
- Kazantzidis, K., Magorrian, J., & Moore, B. 2004, *ApJ*, **601**, 37
- Khochfar, S., & Burkert, A. 2006, *A&A*, **445**, 403
- Krajinović, D., Cappellari, M., Emsellem, E., McDermid, R. M., & de Zeeuw, P. T. 2005, *MNRAS*, **357**, 1113
- Lamb, S. A., Hearn, N. C., & Gao, Y. 1998, *ApJ*, **499**, L153
- Lynds, R., & Toomre, A. 1976, *ApJ*, **209**, 382
- Mahoney, J. M., Burke, B. F., & van der Hulst, J. M. 1987, in *Dark Matter in the Universe, The Mass of the Binary Galaxies NGC4038/39—the Antennae*, ed. J. Kormendy & G. R. Knapp (Dordrecht: Reidel), 94
- McMillan, P. J., & Dehnen, W. 2007, *MNRAS*, **378**, 541
- Mihos, J. C. 2001, *ApJ*, **550**, 94
- Mihos, J. C., & Bothun, G. D. 1997, *ApJ*, **481**, 741
- Mihos, J. C., Bothun, G. D., & Richstone, D. O. 1993, *ApJ*, **418**, 82
- Mihos, J. C., Dubinski, J., & Hernquist, L. 1998, *ApJ*, **494**, 183
- Naab, T., & Burkert, A. 2003, *ApJ*, **597**, 893
- Navarro, J. F., Frenk, C. S., & White, S. D. M. 1996, *ApJ*, **462**, 563
- Noreau, L., & Kronberg, P. P. 1986, *AJ*, **92**, 1048
- Pfleiderer, J., & Seidentopf, H. 1961, *Zap*, **51**, 201
- Quinn, P. J., & Goodman, J. 1986, *ApJ*, **309**, 472
- Salo, H., & Laurikainen, E. 1993, *ApJ*, **410**, 586
- Salo, H., & Laurikainen, E. 2000, *MNRAS*, **319**, 377
- Scharwächter, J., Eckart, A., Pfalzner, S., Zuther, J., Krips, M., & Straubmeier, C. 2004, *A&A*, **414**, 497
- Schwarzschild, M. 1979, *ApJ*, **232**, 236
- Schweizer, F. 1977, in *Structure and Properties of Nearby Galaxies, Galaxies with Long Tails*, ed. E. M. Berkhuijsen & R. Wielebinski (Dordrecht: Reidel), 279
- Smith, B. J. 1994, *AJ*, **107**, 1695
- Smith, B. J., & Wallin, J. F. 1992, *ApJ*, **393**, 544
- Sotnikova, N. Y., & Reshetnikov, V. P. 1998, *Astron. Lett.*, **24**, 73
- Springel, V., & White, S. D. M. 1999, *MNRAS*, **307**, 162
- Stanford, S. A., & Balcells, M. 1991, *ApJ*, **370**, 118
- Stockton, A. 1974, *ApJ*, **187**, 219
- Struck, C. 1997, *ApJS*, **113**, 269

- Struck, C., Kaufman, M., Brinks, E., Thomasson, M., Elmegreen, B. G., & Elmegreen, D. M. 2005, [MNRAS](#), **364**, 69
- Struck, C., & Smith, B. J. 2003, [ApJ](#), **589**, 157
- Struck-Marcell, C., & Higdon, J. L. 1993, [ApJ](#), **411**, 108
- Thies, C., & Kohle, S. 2001, [A&A](#), **370**, 365
- Thies, C., & Spinneker, C. 2003, [Ap&SS](#), **284**, 495
- Theys, J. C., & Spiegel, E. A. 1977, [ApJ](#), **212**, 616
- Thomasson, M., & Donner, K. J. 1993, [A&A](#), **272**, 153
- Toomre, A. 1977, in *Evolution of Galaxies and Stellar Populations, Mergers and Some Consequences*, ed. B. M. Tinsley & R. B. Larson (New Haven, CT: Yale University Press), 401
- Toomre, A. 1978, in *The Large Scale Structure of the Universe, Interacting Systems* (Dordrecht: Reidel), 109
- Toomre, A., & Toomre, J. 1972, [ApJ](#), **178**, 623
- Tully, R. B., & Fisher, J. R. 1977, [A&A](#), **54**, 661
- van Albada, T. S., & van Gorkom, J. H. 1977, [A&A](#), **54**, 121
- van de Ven, G., de Zeeuw, P. T., & van den Bosch, R. C. E. 2008, [MNRAS](#), **385**, 614
- van den Bosch, R. C. E., van de Ven, G., Verolme, E. K., Cappellari, M., & de Zeeuw, P. T. 2008, [MNRAS](#), **385**, 647
- van der Hulst, J. M. 1979, [A&A](#), **71**, 131
- van der Kruit, P. C., & Searle, L. 1981, [A&A](#), **95**, 105
- Vollmer, B. 2003, [A&A](#), **398**, 525
- Vollmer, B., Braine, J., Combes, F., & Sofue, Y. 2005, [A&A](#), **441**, 473
- von Neumann, J. 1951, in *Monte Carlo Method*. National Bureau of Standards Applied Mathematics Series 12 (Washington, DC: US Government Printing Office), 36
- Wahde, M. 1998, [A&AS](#), **132**, 417
- Wahde, M., & Donner, K. J. 2001, [A&A](#), **379**, 115
- Wallin, J. F., & Stuart, B. V. 1992, [ApJ](#), **399**, 29
- White, S. D. M. 1978, [MNRAS](#), **184**, 185
- White, S. D. M. 1979, [MNRAS](#), **189**, 831
- Yun, M. S. 1999, in *Galaxy Interactions at Low and High Redshift, Tidal Interactions in M81 Group*, ed. J. E. Barnes & D. B. Sanders (Dordrecht: Kluwer), 81
- Zhao, H. S. 1996, [MNRAS](#), **278**, 488